THESIS FOR THE DEGREE OF LICENTIATE OF ENGINEERING

Coated Ferritic Stainless Steels as Interconnects in Solid Oxide Fuel Cells

Jan Gustav Grolig

Department of Chemical and Bioengineering
CHALMERS UNIVERSITY OF TECHNOLOGY
Gothenburg, Sweden 2013

Coated Ferritic Stainless Steels as Interconnects in Solid Oxide Fuel Cells
Jan Gustav Grolig

Licentiatuppsatser vid Institutionen för Kemi och Bioteknik
Chalmers Tekniska Högskola
Serie Nr. 2013:23
ISSN: 1652:943X

Department of Chemical and Bioengineering
Division of Energy and Materials
Environmental Inorganic Chemistry
The High Temperature Corrosion Centre
Chalmers University of Technology
SE - 412 96 Gothenburg, Sweden
Phone + 46 (0)31 772 2828

Printed by Chalmers Reproservice
Chalmers University of Technology
Gothenburg, Sweden 2013

Cover: Sample holder with three samples after removal from the furnace.

Coated Ferritic Stainless Steels as Interconnects in Solid Oxide Fuel Cells

Jan Gustav Grolig
Department of Chemical and Bioengineering
Chalmers University of Technology

Abstract

Solid oxide fuel cells (SOFCs) have gained increased research interest as they are promising devices for a decentralized and clean electricity and heat production. Several material challenges have to be solved to reach sufficient efficiencies and life times. One important aspect are ferritic stainless steels as interconnect materials which are corrosion resistant, mechanically stable and cost optimized. This work is aimed to investigate economic solutions for interconnect materials and understand the underlying degradation mechansims. Two substrates, the commercial available steel AISI 441 and the ferritic stainless steel optimized for an SOFC application Sandvik Sanergy HT, were combined with different barrier coatings and exposed in cathode atmosphere.

The ferritic stainless steel AISI 441 coated with different reactive element and reactive element/cobalt coatings was investigated concerning corrosion resistance and chromium volatilization. Uncoated 441 suffered from severe corrosion, which was successfully improved by coatings of cerium and lanthanum. Cerium/cobalt-coated AISI 441 was showing excellent and promising properties for a interconnect application.

Sandvik Sanergy HT coated with novel conversion coatings of copper with manganese or iron was examined in a similar way. Coatings of copper and iron improved the corrosion and chromium evaporation properties significantly and were promising for further developments. In contrast did copper combined with manganese as coating on Sandvik Sanergy HT not result in an improvement in corrosion properties and chromium evaporation.

Keywords: SOFC, Interconnect, Chromium volatilization, Stainless Steel

Appended papers

The thesis is based on the following articles:

- J. G. Grolig, J. Froitzheim and J.-E. Svensson. Coated Stainless Steel 441 as Interconnect Material for Solid Oxide Fuel Cells: Oxidation Performance and Chromium Evaporation *Journal of Power Sources*, accepted for publication, doi:10.1016/j.jpowsour.2013.08.089, 2013.
- J. G. Grolig, H. Abdesselam, M. Gas, H. F. Windisch, J. Froitzheim and J.-E. Svensson. Copper Based Conversion Coatings on Ferritic Stainless Strip Steel as Solid Oxide Fuel Cell Interconnects: Oxidation Performance and Chromium Evaporation *ECS Transactions*, accepted for publication, 2013.

Statement of author's contribution

For both papers I was the main author. In paper A I did the main part of the scientific writing and all the experimental work, except the FIB preparation, that was performed by Dr. M. Sattari. In Paper B most of the experiments were performed by H. Abdesselam and M. Gas and I did only some of the experiments and the main part of the scientific writing.

List of acronyms

ASR	Area Specific Resistance
CGO	Gadolina doped Ceria
CTE	Coefficient of Thermal Expansion
EDX	Energy Dispersive X-ray analysis
FIB	Focused Ion Beam
HTC	High Temperature Corrosion Center
HTPEM	High Temperature Polymeric Membrane Fuel Cell
KMC	Kinetic Monte Carlo Simulation
LSC	Scandia Doped Lanthanum Chromite
LSCF	Strontium Iron Doped lanthanum cobaltite
LSM	Strontium Doped Lanthanum Magnetite
PAFC	Phosphoric Acid Fuel Cell
PEM	Polymeric Membrane Fuel Cell
RE	Reactive Element
SEM	Scanning Electron Microscopy
SOFC	Solid Oxide Fuel Cell
TEM	Transmission Electron Microscopy
YSZ	Yttria stabilized Zirconia

Contents

Acknowledgements

First I would like to thank my main supervisor Prof. Jan-Erik Svensson and my co-supervisor Dr. Jan Froitzheim for providing me with this thesis, helpful advice whenever needed and allowing me to steer my research. Furthermore, I would like to thank Prof. Lars-Gunnar Johansson for being my examiner and for supporting me with his scientific knowledge and input. Prof. Sten Eriksson is acknowledged for being my director of studies.

A special thanks goes to my fellow co-workers in The Fuel Cell Group, Christine, Hannes, Maria, Mohammad, Patrik and Rakshith for supporting me on various issues, creating great team spirit and for withstanding my personality.

In addition, I would like to thank the entire team of the High Temperature Corrosion Center for the work experience of the last two years. The Environmental Inorganic Chemistry Group, especially Martin Keller is tremendously thanked for helping me doing different outgoing experiments. The group of Prof. Elisabet Ahlberg, Dr. Chris Knee and Francis Kinyanjui are acknowledged for providing help and instrumentation for the electrical characterization.

Esa Väänänen and Erik Brunius are acknowledged for their great support in building and fixing new laboratory equipment. Charlotte Bouveng is gratefully acknowledged for her assistance in finding a flat and helping me through different administrative challenges.

Last but not least I would like to thank my family for supporting me in my not always understandable decision to earn a PhD in Sweden.

Chapter 1

Introduction

Global warming is one of the major challenges we face in upcoming decades. The increasing CO_2 emissions have been identified to be one of the major problems causing the green house effect. The reduction of CO_2 emissions combined with the shortage of fossil fuels leads to a demand for new technologies for a clean, more effective and, preferably decentralized, energy production.
Solid oxide fuel cells are one important part of a strategy to meet this demand. They can reach currently electrical efficiencies up to 60 % and allow for the flexible and decentralized production of electricity and heat. Solid oxide fuel cells convert chemical energy stored in a fuel into electricity without combustion. Since they can already operate on existing fuels their boundary to implementation is rather low compared to other fuel cell technologies. There are already some pilot plants in operation that have proven the concept successfully [1].
Several material challenges have to be solved for allowing a large-scale industrial production and implementation of solid oxide fuel cells. Besides more (cost-)effective catalysts, interconnects have gained increased research interest. Interconnects are needed to combine several fuel cell elements to a stack, and they contribute significantly to the total cost of the stack. Ferritic stainless steels have been identified as the material of choice for an interconnect application. The major issues for ferritic stainless steel interconnects are; high temperature corrosion, the volatilization of chromium and the increasing electrical resistance over their lifetime.
Tailor-made alloys have been developed to improve these properties and, in addition, high effective coatings in the range from submicron to micrometers can be applied. The drawback of these solutions is usually meeting the desired costs, therefore either economical alloys have to be used or the coatings have to be improved towards reduced prices.

1.1 Aim of the thesis

The aim of this thesis is the development of new substrate/coating combinations to reach performances similar to state-of-the-art developments by being more cost effective. Two routes were selected; the first one was studying an economical substrate material such as stainless steel AISI 441 with state-of-the-art coatings, and the second one was aimed at developing new copper-based coatings for a state-of-the-art substrate material, such as Sandvik Sanergy HT.
Furthermore it was aimed to investigate the degradation and corrosion mechanisms of both selected steels with and without coatings. Finally developing a method for an electrical characterization on promising steel/coating combinations was planned.

Chapter 2

Theory

2.1 Solid Oxide Fuel Cells

Solid Oxid Fuel Cells (SOFCs) are devices that convert electrical energy directly into electricity from a reaction between a fuel (such as hydrogen) and oxygen without combustion. Their function is based on an oxygen-ion-conducting electrolyte in combination with mixed conducting electrodes. Since the working principle of an SOFC is not a Carnot process, SOFCs reach higher efficiencies than conventional combustion engines. Additionally fuel cells work almost silently and with less pollution (depending on the fuel). Consequently SOFCs are promising devices in a future hydrogen-based economy [2].
The working principle of an SOFC is shown in Figure 2.1 and can be explained as follows: A fuel, in the depicted case hydrogen, is oxidized at the anode side and forms water. The anode side reaction is described in Equation 2.1. The released electrons are transferred through an external circuit to the cathode side. On the cathode side (see Equation 2.2) oxygen uptakes these electrons and is reduced, the formed oxygen ions diffuse, due to the osmotic pressure, through the electrolyte, and react on the anode side with the hydrogen (the overall reaction in Equation 2.3). The electrons that are transferred through the external circuit can be used to drive an electric load [2].

$$\mathrm{H_2} + \mathrm{O^{2-}} \longrightarrow \mathrm{H_2O} + 2\,\mathrm{e^-} \tag{2.1}$$

$$\tfrac{1}{2}\,\mathrm{O_2} + 2\,\mathrm{e^-} \longrightarrow \mathrm{O^{2-}} \tag{2.2}$$

$$\tfrac{1}{2}\,\mathrm{O_2} + \mathrm{H_2} \longrightarrow \mathrm{H_2O} \tag{2.3}$$

Besides SOFCs there are also different other types of fuel cells available. Table 2.1 lists some of the most important fuel cell types and their common characteristics.

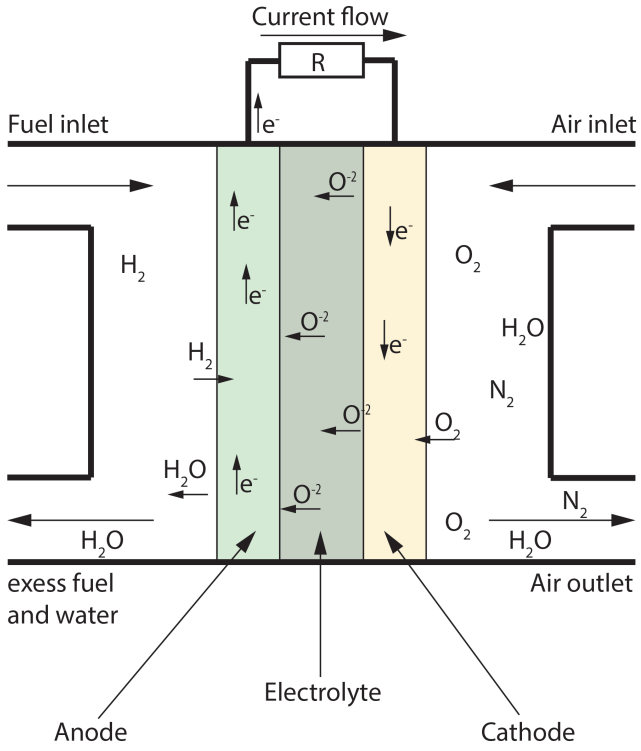

Figure 2.1: Working principle of a solid oxide fuel cell.

In contrast to most other fuel cell types, SOFCs do not require purified hydrogen as a fuel but can run almost on any hydrocarbon fuel. Their relatively high operation temperatures make them most suitable for stationary operation with preferably a low number of start up/shut down cycles. Polymeric Membrane (PEM) and High Temperature Polymeric Membrane (HTPEM) fuel cells, in contrast, allow short start up/shut down times and are subsequently better suited for mobile applications. But due to their utilization of platinum catalysts, which are sensitive to carbon monoxide, they require highly purified fuels [2]. There are different material requirements for the different components of an SOFC, which are described in more detail in the following sections.

2.1.1 Electrolyte materials

The electrolyte of an SOFC has to be conductive for oxygen ions, it should be non-conductive for electrons and stable both in oxidizing and reducing environments [3]. The most common electrolyte material is Yttria Stabilized Zirconia (YSZ), but other choices such as Gadolina Doped Ceria (CGO) have been reported as effective, too. Undoped zirconia has up to a temperature of 1170 °C a monoclinic crystal structure and by doping zirconia with yttria, or other aliovalent oxides, oxygen vacancies are introduced and the crystal structure is modified to the cubic fluorite structure [3, 4]. The oxygen conductivity of YSZ can be increased by increasing the doping level of

Type	Temp. °C	Fuel	Electrolyte	Mobile ion	Advantages	Disadvantages
PEM (polymeric membrane fuel cell)	70 - 110	Hydrogen	Sulfonated polymers (Nafion®)	H^+	quick start up	high purity fuels required, platinum catalysts
HTPEM (high temperature polymeric membrane fuel cell)	150 - 200	Hydrogen	Phosphoric acid doped polybenzimidazole (PBI)	H^+	quick start up	phosphoric acid release, platinum catalysts
PAFC (phosphoric acid fuel cell)	150 - 250	Hydrogen	Phosphoric acid	H^+	high tolerance against CO	only constant operation
SOFC (solid oxide fuel cell)	600 - 800	Hydrocarbons, CO	YSZ, CGO	O^{2-}	high fuel tolerance	no quick start up, high operation temperatures

Table 2.1: Common fuel cell types and their characteristics, adapted from [2]

yttria. A maximum oxygen ion conductivity is reached with an yttria content of about 8.3 wt. % (a graph representing the oxygen ion conductivity enhancement is shown in Figure 2.2). Doping with yttria increases the number of oxygen vacancies and thus increases the diffusion constant of oxygen within the zirconia. Due to the the higher probability to hit a Y-Y pair, which has a higher binding energy with oxygen, the average hopping energy for oxygen increases. The optimum yttria concentration with the highest oxygen ion conductivity has been proven to be around 8.3 % [3].

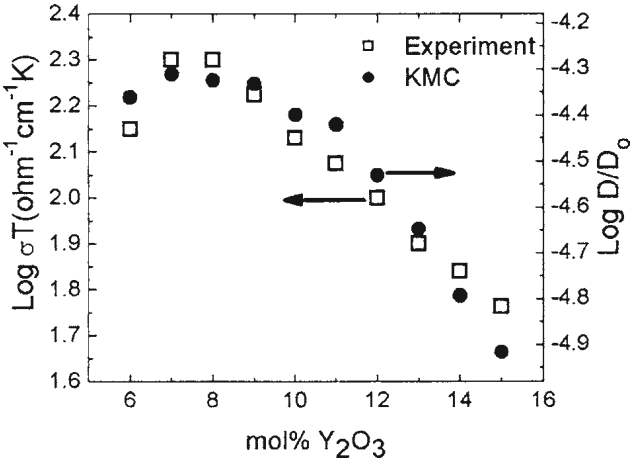

Figure 2.2: Oxygen ion conductivity and diffusion constant of zirconia with varying yttria doping, experimental values and kinetic monte carlo simulation (KMC), taken from [5]

CGO in contrast has a higher electronic conductivity when exposed to reducing environments at elevated temperature. The higher electronic conductivity leads to increased leakage currents and thus decreases the power output of the fuel cell. At

temperatures below 500 °C the electronic conductivity of CGO gets low enough to make it a promising candidate for low temperature SOFCs. Typical doping levels of CGO are in the range of 20 wt. %.
Other potential electrolyte candidate materials are Scandia Doped Zirconia, which performs similar to YSZ but is more expensive, or strontium- and magnesium- doped lanthanum gallate $LaGaO_3$, which is promising for a temperature range between $600 - 700\,°C$ but suffers from phase instability which negatively affects its long-term durability [3].

2.1.2 Electrode materials

Generally both electrodes should conduct both ions and electrons. The anode has to be catalytically active in oxidizing the fuel, whereas the cathode has to be effective in reducing oxygen.

Anode materials

The anode of an SOFC has to be stable at relatively high operation temperatures and in reducing anode environments. It has to be catalytically active to oxidize the fuel and it should be porous to allow for the flow of gas to and the removal of the reaction products from the electrolyte [6]. The porosity of the anode should be maintained during the whole lifetime of the fuel cell; in other words any sintering effects of the pores should be inhibited. Material choices for SOFC anodes are mostly nickel, cobalt or precious metals. Due to the high price of cobalt and precious metals the most commonly used anode material is nickel [4]. Nickel is usually combined with YSZ to achieve the desired mixed conducting properties. The challenge in combining nickel with YSZ is the miss-match of the thermal expansion coefficient. A common way to solve this issue is incorporating nickel particles into a YSZ matrix and forming a so-called cermet. By increasing the nickel content in the cermet the electrical conductivity and also the thermal expansion coefficient are increased. The nickel content in the cermet has to be just above 30 vol. % to avoid cracking with the electrolyte, due to the increased thermal expansion coefficient, and to ensure a sufficiently high electrical conductivity [4, 6].

Cathode materials

The cathode of an SOFC has to be both ionic and electronically conductive, it also has to be porous and stable at the high operation temperatures [6]. In contrast to the anode, its stability has to be maintained in oxidizing environments. Potential cathode materials range over a wide choice of mixed oxides, since all stable (noble) metals are excluded for economic reasons. The most commonly reported cathode material is Strontium Doped Lanthanum Magnetite (LSM) [3]. Besides LSM there are alternative materials such as doped lanthanum cobaltite ($LaCoO_3$) which is co-doped with strontium and iron to form $La_{1-x}Sr_xCo_{1-y}Fe_yO_3$ (LSCF). Compared to

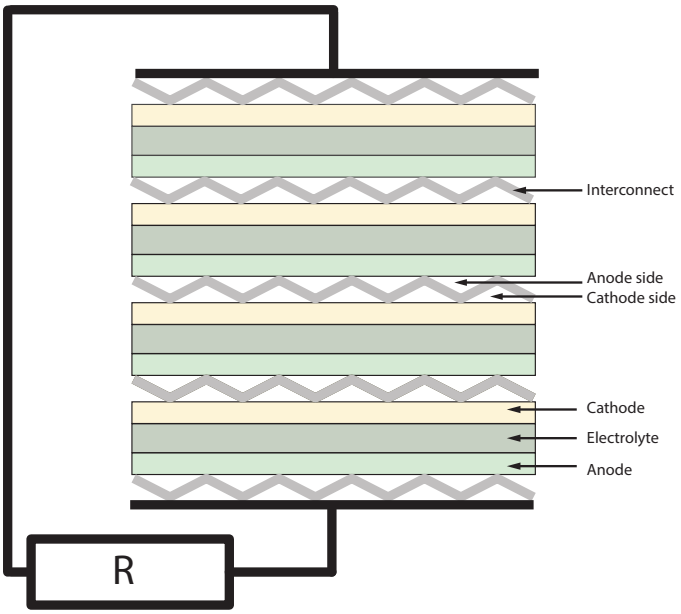

Figure 2.3: Schematic diagram of a planar SOFC stack

LSM, LSCF shows a higher electrical conductivity but also tends also to react with the electrolyte, which makes it only promising for use as a cathode at intermediate temperatures [3].

2.1.3 Interconnects

A single fuel cell element usually produces less than 1 V of electrical potential, depending on the fuel cell effectivity and the fuel utilization. Since 1 V of voltage output is rather inconvenient for most applications and for reaching a higher power density, several fuel cell elements must be combined together. Therefore, planar fuel cell elements are usually placed on top of each other to form a so-called stack. A connecting part is needed between each fuel cell element in order to connect the two cells electronically and to separate the cathode atmosphere of one cell from the anode atmosphere of the next cell. These connecting elements are called interconnects or bipolar plates (the latter term mainly used for PEMFCs). A sketch of an SOFC stack using planar fuel cell elements in combination with interconnects is shown in Figure 2.3 [7, 8].

The requirements on interconnects are a similar thermal expansion coefficient, good electrical conductivity, gas tightness, stability at the SOFC-operating temperatures and in the respective atmospheres [7–9]. To allow for feasible mass production, the interconnects should also be cost effective. In early SOFCs, thick ceramic interconnect plates were employed which had a high weight, required extensive machining and high operation temperatures to be sufficiently conductive. Due to recent improvements in electrolyte and electrode research, the operation temperatures have been lowered to allow the utilization of metallic interconnects.

Ceramic interconnect materials

Ceramic interconnects offered the advantage of a similar thermal expansion coefficient and relative high stability, both in anode and cathode atmospheres. Almost only lanthanum chromite, doped either with CaO or SrO, meets the requirements for an interconnect application. In comparison to metallic interconnects, lanthanum chromite is expensive and less mechanical stable [9, 10]. Moreover, the electrical and heat conductivity of the p-type conducting material are far lower than those of metallic materials [11].

Ferritic stainless steels

Ferritic stainless steels suitable for an interconnect application contain chromium between 10 and 26 wt. % and are usually relatively stable at high temperatures. Their crystal structure is body-centered-cubic and they have a matching coefficient of thermal expansion (CTE) of about 10 x 10^{-6}/K. For SOFCs, alloys with a chromium content between 18 and 23 wt.% have shown promise. Examples of specially developed alloys for an SOFC interconnect application are Crofer 22 APU and Crofer 22 H from ThyssenKrupp VDM, Sandvik Sanergy HT from Sandvik Materials Technology or ZMG 232 G10 from Hitachi Metals [12–14], which have been optimized for corrosion protection, mechanical properties and chromium evaporation. More detailed information about challenges for metallic interconnects can be found in section 2.3.

2.2 Corrosion of metals

Corrosion is the gradual degradation of a material (mainly metals) through reaction with its environment. Generally corrosion can be classified into two areas which are aqueous or atmospheric corrosion and high temperature corrosion. Atmospheric corrosion occurs already at very low temperatures and it always involves some kind of electrolyte. High temperature corrosion in contrast entails reactions between metals and their surrounding gas phase. For the metallic interconnects used in SOFCs, the relevant corrosion processes are limited to high temperature corrosion, which is the focus of the following sections.

2.2.1 Thermodynamics

At high temperatures metals can directly react with their surrounding gas phase to form products such as oxides, carbides, nitrides or sulphides [15]. The reaction between oxygen and a metal can be written as in Equation 2.4. It can only occur if the free enthalpy ΔG° is negative. As the reaction involves oxygen, an equilibrium oxygen partial pressure can be expressed as shown in Equation 2.5. If the pressure is lower than the equilibrium partial pressure, no oxide will be formed; at higher partial

pressures the reaction is thermodynamically favored.

$$\frac{2x}{y}\mathrm{M} + \mathrm{O}^2 \longrightarrow \frac{2}{y}\mathrm{M_xO_y} \tag{2.4}$$

The term a_M describes the thermodynamic activity of the metal (1 for a pure metal), $a_{M_xO_y}$ is the thermodynamic activity for the oxide in a solid solution of oxides [16].

$$pO_2 = \frac{a_{M_xO_y}^{2/y}}{a_M^{2x/y}} \exp(\Delta G^\circ / RT) \tag{2.5}$$

To predict oxide formation of a specific metal at a specific temperature and in a specific partial oxygen pressure Ellingham/Richardson diagrams can be used. This kind of diagram was first introduced by Harold J.T. Ellingham in 1944 [17]. It combines the free enthalpy ΔG° with the corresponding equilibrium partial pressure of oxygen over different temperatures. More stable oxides are plotted in the lower part of the Ellingham/Richardson diagram. A simplified Ellingham/Richardson diagram is shown in Figure 2.4. It not only helps in predicting whether or not a specific oxide on a metal will form, but it also can be useful in predicting which oxides will form on an alloy (at a given temperature and atmosphere).

2.2.2 Kinetics

As described in the previous section, it is possible to predict whether or not specific oxidation reactions will be thermodynamically favored or not. The thermodynamic predictions do not give any information about the reaction rate or if an oxidation reaction will take place at all.
The oxidation of a metal can be divided into two steps, which are illustrated in Figure 2.5. First an initial oxidation, in which an unoxidized (blank) metal is exposed to an oxidizing atmosphere, and second, the long-term oxidation process in which an oxide scale on a metal grows due to solid state diffusing oxygen and metal ions. In the first moments of exposing a metal to a high temperature and an oxidizing environment, oxygen atoms are adsorbed on the metal's surface. These oxygen atoms are then reduced and begin forming oxide islands. After a some time these oxide islands grow until the entire surface is covered with oxide. The metal consequently is then separated by an oxide scale from the atmosphere. To further oxidize the metal, either metal ions have to diffuse through the oxide to the outer surface or oxygen ions have to diffuse through the oxide scale to the metal interface. Both diffusion processes can also happen in parallel. Depending on the predominant diffusion process, one can classify these as outward growing oxide scales (metal outward diffusion) or inward growing oxide scales (oxygen ion inward diffusion) [15].
A common way to measure the corrosion rate of a metal and to predict its life time is monitoring the mass change of a sample over exposure time. This can be done in-situ during exposure with thermogravimetry, but also in a post analysis. The mass

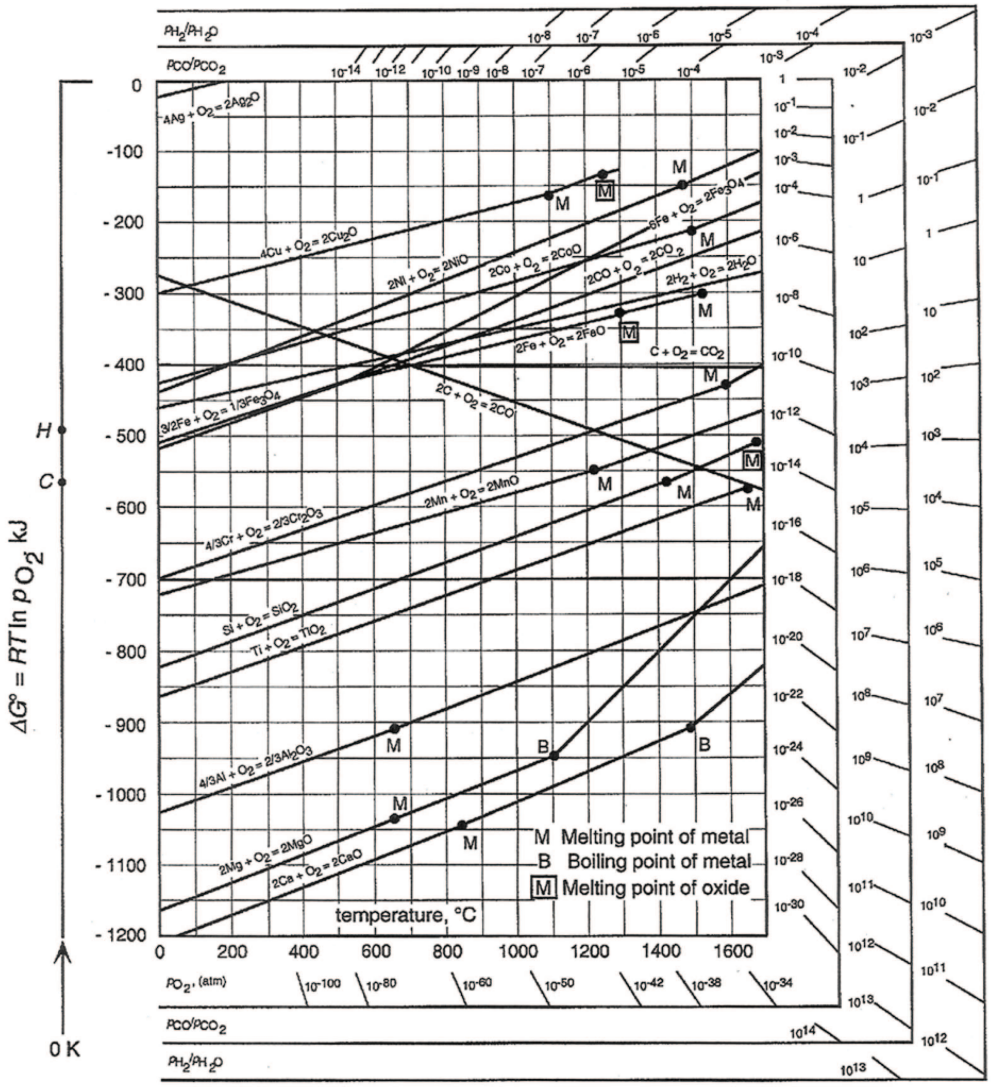

Figure 2.4: Ellingham/Richardson diagram for various metals, taken from [18]

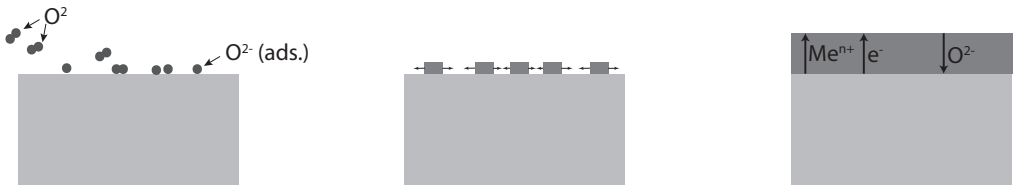

Figure 2.5: Step-wise oxide scale formation; from oxygen adsorption, oxide nucleation and oxide scale growth adapted from [15].

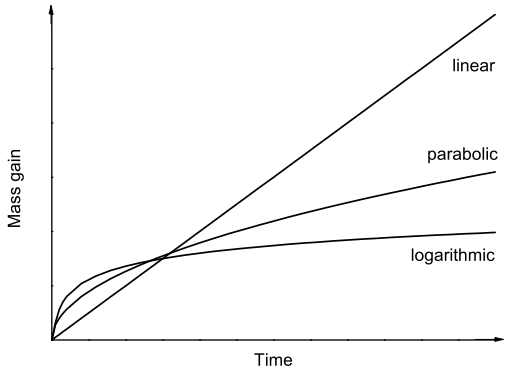

Figure 2.6: Mass gain curves for three common oxidation mechanisms, adapted from [19]

change is, if no volatilization or oxide scale spallation processes are involved, equal to the oxygen uptake and metal consumption. Depending on the oxidation process one can distinguish between different oxide growth mechanisms: Such as parabolic, logarithmic or linear mechanisms, see Figure 2.6.

Parabolic mechanism

A parabolic oxidation process depends on solid state diffusion and it can be expressed with a theory introduced by C. Wagner. The model was first introduced in 1933 and is based on the following assumptions: A well adhered oxide scale is formed, the growth rate is determined by solid state diffusion, local equilibria at the metal/oxide interface and at the gas/oxide interface and finally oxygen solubility in the metal is negligible [20]. Since the growth rate is only dependent on the diffusion of ions or electrons through the oxide scale, the rate will decrease with time due to the increasing length of the diffusion paths. The oxide thickness increases parabolic with time and can be expressed using the Formulas 2.6 and 2.7 [15].

$$dx/dt = k'_p * 1/x \tag{2.6}$$

$$x^2 = 2k'_p + C \tag{2.7}$$

Where x is the oxide thickness, t is the time, k'_p is the parabolic rate constant and C is the integration constant. Parabolic oxidation behavior is often a desired mechanism since it is the result of a protective oxide scale.

Logarithmic mechanism

Logarithmic oxide scale growth can be observed at temperatures below 400°C and after a fast initial oxidation the reaction rate drops down to almost insignificant rates. There is no general consensus about the reaction mechanism for logarithmic oxidation.

Potential explanations for the rate determing step are ion or electron transport due an electric field, chemisorption or cavity formation within the oxide film [21].

Linear mechanism

If the mass gain curve follows a linear trend, the oxide scale has no protective properties. The rate of reaction stays constant and is independent of the amount of gas or metal consumed. This is usually the case if the rate-controlling step within the reaction is a surface or phase boundary process [15].

Break-away corrosion

Break-away corrosion is used as a synonym for a combination of two rate equations. Break-away corrosion can happen after an initial parabolic oxidation process, which is then followed by a linear oxidation process. The protective oxide scale breaks down after some time and is then not protective anymore. This break-down of a protective oxide scale can be observed if an alloy is depleted in protective oxide forming atoms [15].

2.3 Interconnect-related corrosion challenges

Ferritic stainless steels used as metallic interconnects for SOFCs face three major challenges: Degradation due to corrosion; the evaporation of chromium and the increase in electrical resistance due to the growing chromia scale. Besides optimizing the alloy composition, several studies have shown, that additional coatings are effective in improving the interconnect performances. The following sections will describe the specific main challenges for interconnects and some solutions in more detail. Since the focus of this thesis is on the cathode side improvements, the following sections will deal with problems related to the cathode side.

2.3.1 Corrosion

On the cathode side the interconnect is exposed to an air atmosphere, that is, due to humidity, also containing a small amount of water. Several measures are known to prevent rapid oxidation in this atmosphere. Most common is designing alloys to form protective oxide scales which are slow growing and well adhered to the metal. Examples of protective scales are alumina or chromia, in rare cases also silica-forming alloys. As previously mentioned chromia formers are the only material considered for an interconnect application, both alumina and silica formers are, due to their high resistivity, unsuitable as interconnects. As long as the steel still contains sufficient amounts of chromium the protective scale will continue to grow. When due to oxidation or volatilization of chromium (see section 2.3.2) the chromium content in the steel is below a certain limit, rapid break-away oxidation can occur. Depending on the

used alloy and experimental conditions this limit is reached at a chromium content below approximately 16% [22]. The problem of chromium depletion can be increased by using very thin interconnects and therefore reducing the chromium reservoir in the interconnect.
Another observed corrosion problem of interconnects is so-called spallation of the oxide scale. There are various reasons for oxide scale spallation. A missmatch of the thermal expansion coefficients (CTE) between the metal and the scale, growth stresses during oxidation or poor scale adhesion due to debonding of the oxide from the metal . Some researchers also proposed subscale silica formation as reason for oxide scale spallation [8, 12, 23].

Reactive Elements

Besides designing alloys to form protective oxide scales that prevent the metal from break-away corrosion, so-called reactive elements can be added to the alloy. Reactive elements belonging to the rare earth elements such as cerium, lanthanum, yttrium or zirconium and are known to improve the corrosion resistance of alumina and chromia forming alloys significantly when added in small quantities [24]. There is proposed that additions of atoms with a high mass and high oxygen affinity are more beneficial for the protection of an alloy [25]. Up to now there is no clear consensus on the mechanism of the reactive element effect. Proposed by Wittle and Stringer in 1980 [25] and revised by Pint in 2001 [24] there are different suggestions why reactive elements enhance corrosion resistance. There have been discussions for decades about the so-called reactive element effect. Several mechanisms have been proposed to explain the beneficial effect of reactive elements. The most discussed effects are a change in the oxide growth mechanism, improvement in the chemical bonding between substrate and oxide or a change of the oxygen vacancy diffusion (the so-called vacancy sink model).

Reactive Element coatings

It has been shown that even a very thin coating of reactive elements can have the same beneficial effect on corrosion as small additions to the alloy [23, 26–28]. Fontana et al. have shown improved corrosion resistance and oxide scale adhesion of selected chromia forming alloys such as Crofer 22 APU, AL452 and Haynes 230 with RE coatings of neodymium, lanthanum or yttrium oxides [26]. Alman et al. have reported on slower oxidation and improved scale adhesion for cerium coated Crofer 22 APU [23].

2.3.2 Chromium evaporation

Chromium oxide is thermodynamically unstable in humid conditions at high temperatures, and this leads to evaporation of volatile chromic species. It has been shown that there are different volatile species involved in the degradation process, such as CrO_3, $CrO_2(OH)_2$ and $CrO_2(OH)$. The following reactions are involved to

form these species, see Formulas 2.8 - 2.10. Ebbinghaus et al. [29, 30] have proposed that the predominant reaction involved in chromium evaporation is 2.9. This is valid for temperatures below 1800 °C and in atmospheres containing oxygen and water vapor. Opila et al revised this to temperatures up to 900 °C. Chromium evaporation is influenced by various factors, such as temperature, water vapor content or oxygen pressure. In an SOFC application in which high flows are applied, the chromium evaporation can even be increased since the constant gas exchange prevents reaching a chromium saturated gas phase, thus no equilibrium.

$$\tfrac{1}{2}\,Cr_2O_3(s) + \tfrac{3}{4}\,O_2(g) \longrightarrow CrO_3(g) \tag{2.8}$$

$$\tfrac{1}{2}\,Cr_2O_3(s) + H_2O(g) + \tfrac{3}{4}\,O_2(g) \longrightarrow CrO_2(OH)_2(g) \tag{2.9}$$

$$\tfrac{1}{2}\,Cr_2O_3(s) + \tfrac{1}{2}\,H_2O(g) + \tfrac{1}{2}\,O_2(g) \longrightarrow CrO_2(OH)(g) \tag{2.10}$$

Coatings for preventing Chromium evaporation

Various coatings have been reported to be effective in preventing or at least decreasing the volatilization of chromium. They generally can be classified into perovskite structure and spinel structure coatings. Examples of perovskite coatings are LSC ($LaScCrO_3$), LSM ($LaSrMnO_3$) or LSCF ($LaSrCoFeO_3$) [31–33]. They usually have to be applied rather thick and often suffer from poor adhesion to the substrate.
Spinel coatings are mostly based on cobalt, often combined with other transition metals to obtain a cobalt manganese top oxide. Cobalt spinel coatings decrease the evaporation of chromium by a factor of 10 [34]. There has been extensive research on different thin film coating technologies for applying spinel coatings. They can be differentiated into conversion coatings (coatings applied as metals) or oxide coatings (coatings that are already deposited as spinel oxide). The advantage of conversion coatings is that they can be applied very thin and can be deformed without detaching from the substrate [35]. Most spinel coatings usually show good electrical conductivities, see also section 2.3.3 [36].

2.3.3 Electrical conduction of oxide scales

Electrical conduction between the stacked fuel cell elements is one of the key features of an interconnect. The main challenge for the interconnect's conductivity is the growing oxide scale, which is far less electrically conductive than the underlying steel. Therefore it is most important to focus on the oxide scale to improve the interconnect's electronic properties [28].
Generally the conduction of any material can be described using the Formula 2.11.

$$\sigma = \sum \mu_i * n_i * q_i \tag{2.11}$$

$$\sigma = \sigma_0 * e^{\frac{-E_a}{R*T}} \tag{2.12}$$

Where μ_i is the mobility of charge carrier i, n_i is the number of charge carrier i and q_i is the charge of charge carrier i. Different types of charge carriers come into account for oxides, such as electrons, electron holes, ions or ion holes.
Temperature affects the mobility μ_i of electrons usually negatively and ions positive, whereas the charge carrier concentration n_i increases with higher temperature. Oxides usually show an increase in conductivity at higher temperatures due to the fact that the generation of more charge carriers superimpose the decreased electron mobility. This is in contrast to metals in which the decreased electron mobility μ_i outweighs the increased charge carrier generation. The temperature dependence of the conductivity of oxide scales can also be expressed using the Arrhenius relation, (see Equation 2.12). The activation energy is, in addition to the total conductivity, an important material property for identifying which phases of a microstructure contribute most to conduction. [37]

Electric properties of chromia

Since only chromia forming alloys are taken into consideration for an interconnect application, the electrical properties of the interconnect are also heavily determined by the growing chromia scale. At temperatures below 1000 °C pure chromia is known to be p-type conducting and the conductivity of chromia is dependent on the partial pressure of oxygen [38]. The type of electrodes that are used for the characterization also influences the conductivity and activation energy [39]. The activation energy of a grown chromia scale at atmospheric oxygen pressure and temperatures below 1000 °C is in the range of 0.8 eV to 1 eV [40].
The conductivity and also activation energy of chromia is largely dependent on its purity. Several researchers have reported on higher conductivities by doping chromia with nickel, yttrium or magnesium [41, 42].

Electric properties of spinels

The most commonly suggested alloys for an SOFC interconnect application are designed to form a chromium manganese spinel as the outer oxide layer. The conductivity of this chromium manganese spinel is generally higher than that of pure chromia. The electrical conductivity of chromium manganese spinel increases with higher manganese content, while the activation energy decreases with increasing manganese content [43]. As described in the previous section 2.3.2, additional coatings for decreasing the evaporation of chromium are inevitable. The most promising coatings for lowering chromium evaporation are cobalt spinels coatings, but others such as copper spinels have been considered, too. Since all barrier coatings are oxidized before, or in the very first moments of exposure, it is necessary that they are good

	Mg	Mn	Co	Ni	Cu	Zn
Al	$MgAl_2O_4$ $\sigma = 10^{-6}$ $\alpha = 9.0$	$MnAl_2O_4$ $\sigma = 10^{-3}$ $\alpha = 7.9$	$CoAl_2O_4$ $\sigma = 10^{-5}$ $\alpha = 8.7$	$NiAl_2O_4$ $\sigma = 10^{-4}$ $\alpha = 8.1$	$CuAl_2O_4$ $\sigma = 0.05$ $\alpha = -$	$ZnAl_2O_4$ $\sigma = 10^{-6}$ $\alpha = 8.7$
Cr	$MgCr_2O_4$ $\sigma = 0.02$ $\alpha = 7.2$	$Mn_{1.2}Cr_{1.8}O_4$ $\sigma = 0.02$ $\alpha = 6.8$	$CoCr_2O_4$ $\sigma = 7.4$ $\alpha = 7.5$	$NiCr_2O_4$ $\sigma = 0.73$ $\alpha = 7.3$	$CuCr_2O_4$ $\sigma = 0.40$ $\alpha = -$	$ZnCr_2O_4$ $\sigma = 0.01$ $\alpha = 7.1$
Mn	$MgMn_2O_4$ $\sigma = 0.97$ $\alpha = 8.7$	Mn_3O_4 $\sigma = 0.10$ $\alpha = 8.8$	$CoMn_2O_4$ $\sigma = 6.4$ $\alpha = 7.0$	$NiMn_2O_4$ $\sigma = 1.4$ $\alpha = 8.5$	$Cu_{1.3}Mn_{1.7}O_4$ $\sigma = 225$ (750 °C) $\alpha = 12.2$	$ZnMn_2O_4$
Fe	$MgFe_2O_4$ $\sigma = 0.08$ $\alpha = 12.3$	$MnFe_2O_4$ $\sigma = 8.0$ $\alpha = 12.5$	$CoFe_2O_4$ $\sigma = 0.93$ $\alpha = 12.1$	$NiFe_2O_4$ $\sigma = 0.26$ $\alpha = 10.8$	$CuFe_2O_4$ $\sigma = 9.1$ $\alpha = 11.2$	$ZnFe_2O_4$ $\sigma = 0.07$ $\alpha = 7.0$
Co		$MnCo_2O_4$ $\sigma = 60$ $\alpha = 9.7$	Co_3O_4 $\sigma = 6.7$ $\alpha = 9.3$			

Table 2.2: Specific conductivities σ (given in S/cm) and thermal expansion coefficients α (given in ppm/K) of different spinels at 800 °C, except where noted, taken from [36]

conductors. Petric et al. have done an extensive study on the conductivity of different spinels. Table 2.2 lists conductivities and the coefficients of thermal expansion at 800 °C (except where noted) of different transition metal spinels [36].
They concluded in their study that spinels formed of cobalt manganese, copper manganese and copper iron, are from the conductivity and thermal expansion point of view, most promising for an interconnect coating.

Chapter 3

Materials and Methods

3.1 Investigated materials

As first investigation was dealing with the stainless steel 441 as potential candidate for an SOFC interconnect application. The composition of the material is given in Table 3.1. The material was investigated in its uncoated form and with two different coatings of reactive elements; lanthanum and cerium, and two combinatorial coatings of the same reactive element coatings in combination with a cobalt barrier coating. The five different sample sets with each of their coating thicknesses are given in Table 3.2. The investigated coatings have been previously investigated at the high temperature corrosion center (HTC) and have been proven to be effective on Sandviks Sanergy HT [35].

		Fe	Cr	C	Si	Mn	Nb	Ti	P	Ni	Mo	Cu	RE
AISI 441	wt.%	bal.	17.83	0.012	0.55	0.26	0.48	0.14	0.024	0.13			no
Sandvik Sanergy HT	wt.%	bal.	22.4	0.01	0.07	0.25	0.4	0.06	0.13	0.8	0.9	0.017	0.06

Table 3.1: Materials composition, values given from manufacturer.

Sample designation	Inner coating	Outer coating
uncoated		
ce coated	10 nm cerium	-
la coated	10 nm lanthanum	-
ce/co coated	10 nm cerium	620 nm cobalt
la/co coated	10 nm lanthanum	620 nm cobalt

Table 3.2: Investigated coating systems in the first study.

In a second investigation Sandviks Sanergy HT was selected as the substrate material. The composition of the material is given in Table 3.1 and the investigated coating systems are given in Table 3.3. It was tried to form different copper spinels, such as copper manganese or copper iron spinels, that have been identified for having good conductivities and a matching CTE (see section 2.3.3). The atomic ratio between manganese/iron and copper was set to 2:1 by adjusting the thicknesses. The aim was to achieve a similar coating thickness of about 1.2 μm for all coatings.

Sample designation	Inner coating	Outer coating
Mn/Cu	830 nm manganese	400 nm copper
Fe/Cu	800 nm iron	400 nm copper
Cu/Fe*	400 nm copper	800 nm iron

Table 3.3: Investigated coating systems in the second study. *A 50 nm thick Fe strike coating was applied prior to the copper coating.

3.2 Sample preparation

All investigated materials were received in sheets of 0.2 mm thickness from Sandvik Materials Technology AB. The coatings were prepared via an industrially available physical vapor deposition process, and this was also done by Sandvik Material Technology AB. The received sheets were cut into samples of 15 x 15 mm^2 using either a scissor or a metal-cutting tool. Afterwards a cleaning procedure, first in acetone and then in ethanol using ultrasound, was performed. The samples were subsequently weighed using a Satorius MC 5 micro-balance.

3.3 Exposure

Tubular furnaces were used to expose the samples to an SOFC cathode side environment. A scheme of the experimental setup is shown in Figure 3.1. The gas flow was set to a value of 6000 ml/min, and the gas was humidified using a heated water wash bulb in combination with a spiral cooler. The spiral cooler was set to a dew point of 24.4°C to ensure a water content of 3 %. When measuring the mass gain, up to 6 samples were exposed in one run. Only 3 samples were exposed simultaneously for chromium evaporation measurement. The evaporation of chromium was measured using the denuder technique.

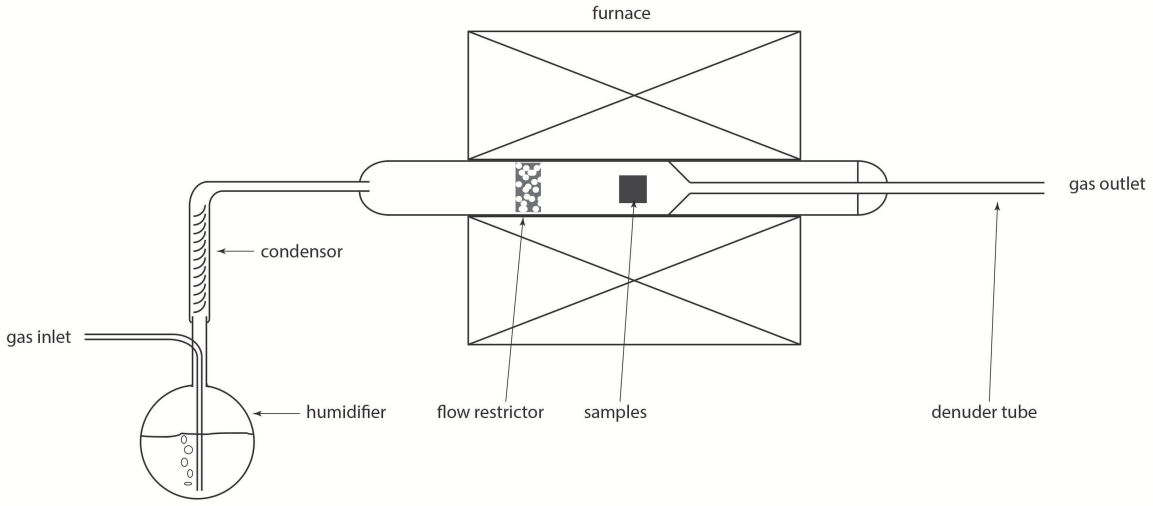

Figure 3.1: Scheme of experimental setup.

3.3.1 Denuder technique

In this study the denuder technique, developed at Chalmers University of Technology, was used to quantify the amount of volatilized chromium. The technique utilizes a tubular furnace setup as shown in Figure 3.1. The outlet of the furnace is equipped with a so-called denuder tube. The exhaust gas is led through this denuder tube which is coated on the inside walls with sodium carbonate. The sodium carbonate reacts with the evaporated chromium species as shown in Formula 3.1.

$$CrO_2(OH)_2 + Na_2CO_3 \longrightarrow Na_2CrO_4 + H_2O + CO_2 \tag{3.1}$$

The denuder tubes can then be changed at regular time intervals, thus allowing a time-resolved measurement of chromium evaporation. The removed denuder tubes were leached out with MQ water. The wash-out solutions were then quantified for chromium concentration using a photo spectroscope. The concentration dependency of the absorption was calibrated using a potassium dichromate solution at different concentrations. The absorption was measured between 0.05 and 2.1 a.u. and showed a linear dependency on the chromium concentration (see Figure 3.2). All chromium evaporation experiments were managed to maintain the measured concentrations between the calibrated values. The absorption factor was calculated to 0.04043 based on chromate concentration [ppm].

3.4 Analytical techniques

The samples were post analyzed mainly using Scanning Electron Microscopy (SEM), but also EDX and electrical characterizations were carried out for selected samples.

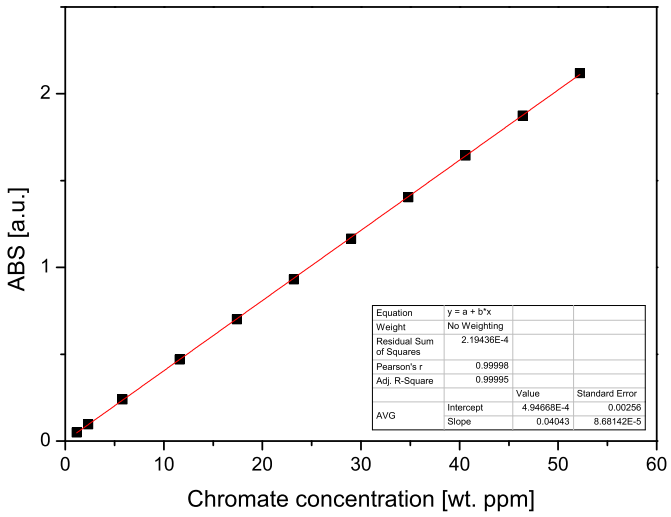

Figure 3.2: Linear dependency of concentration and absorption.

3.4.1 Scanning electron microscopy

In an SEM a focused electron beam is scanned over the surface of the sample. By interacting with the atoms of the sample different emissions are excited. These emissions are, for example, secondary electrons, back-scattered electrons, auger electrons or X-ray emissions, see Figure 3.3. Depending on the detector, these emissions can be transformed into a signal which is then used to create a digital image of the sample [21].
During this thesis mainly secondary and back-scattered electrons were used to image the investigated samples. X-ray emissions were used to determine the composition of the sample. Depending on the used signal a different interaction volume has to be taken into account. A scheme of the interaction volume is shown in Figure 3.4 [19,44].

Secondary electrons

Secondary electrons (SE) are generated when an incoming electron of the electron beam interacts with the electrons of an atom in the sample. The incoming electron is scattered at the electron shell and the released energy is compensated by releasing a second electron. These electrons usually have energies below 50 eV, which is rather low. As seen in Figure 3.4 are secondary electrons relatively surface sensitive and can especially be used for imaging surface topography [19, 44].

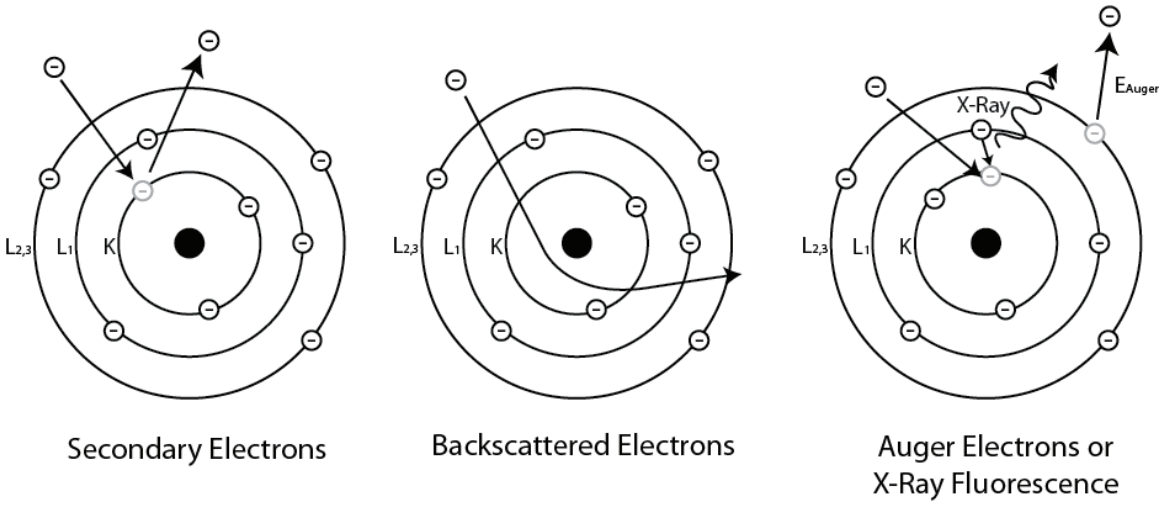

Figure 3.3: Electron atom interactions taken from [45].

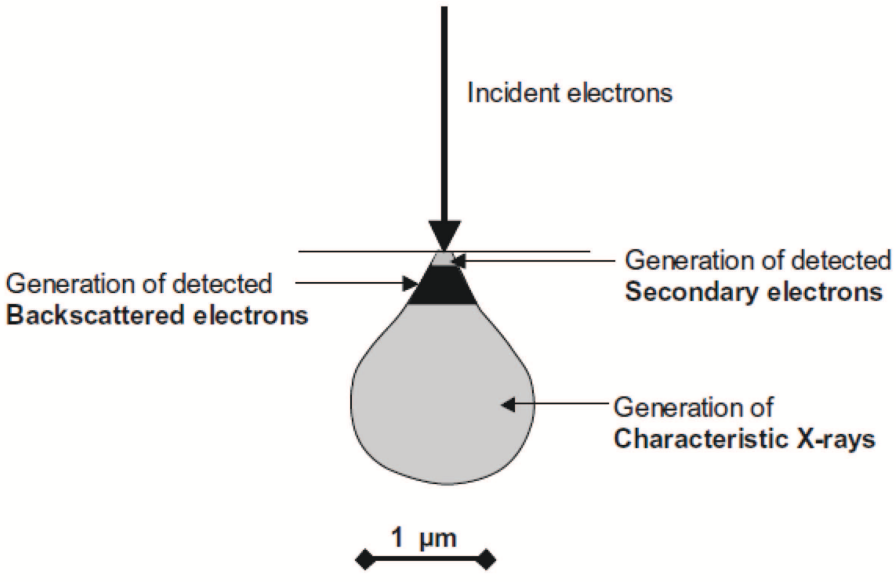

Figure 3.4: Interaction volume of incoming electron beam with sample volume [46].

Back-scattered electrons

Back-scattered electrons are produced when an incoming electron is elastically scattered at an atom core. They are relatively high energetic with energies up to the accelerating voltage of the incoming electron beam, which increases the interaction volume compared to secondary electrons. Due to the higher interaction volume, the resolution and the topographic contrast decreases. A higher atomic number leads to a more effective back-scattering, leading to a compositional contrast, which cannot be observed by using secondary electrons [19, 44].

Energy dispersive X-Ray analysis

Another mechanism in the interaction of the incoming electrons with the electron shell of an atom is the emission of characteristic X-rays. This process occurs when an electron of the inner atom shell is emitted, an electron of the outer electron shell fills the space and the energy difference is compensated by X-ray emission. Due to the specific energies related to the different shells, only X-rays with specific energies are generated. These specific energies can be used to identify the composition of the sample [19, 44].

Focused Ion Beam milling

A Focused Ion Beam (FIB) system works similar to a SEM but instead of electrons, ions are used, most commonly gallium ions. These ions can, in contrast to electrons, be used to erode and deposit material as well as for imaging purposes. Machines with combined SEM and FIB properties allow the preparation of very fine and clean samples for SEM or Transmission Electron Microscopy (TEM) analysis [19, 44].

3.4.2 Electrical Characterization

Different measures have been tried for the electrical characterization. The major challenge in measuring the electrical resistance of an oxidizing steel plate is manufacturing suitable electrodes. The most effective solution was electrodes of sputtered platinum with a painted platinum coating on top of the electrode. The electrode preparation procedure is shown in Figure 3.5. A sputter mask of 10 x 10 mm^2 was placed on a preoxidized sample, and the sample was then sputtered with platinum for 10 min using a Quorum 150 sputter coater and a sputter current of 60 mA. The procedure was then repeated for the back-side of the sample. After sputtering, the electrodes were re-painted with platinum paste (Metalor 6082) using a fine brush. To remove the binder from the platinum paint, the samples were fired at 850°C in air with a peak time of 10 min.
A Probostat (NorECs, Norway) test cell, placed in a tubular furnace, was used to connect the sample to a Solartron 1260A impedance analyzer. The resistance of each sample was measured at temperatures between $900 - 500$°C. The impedance analyzer

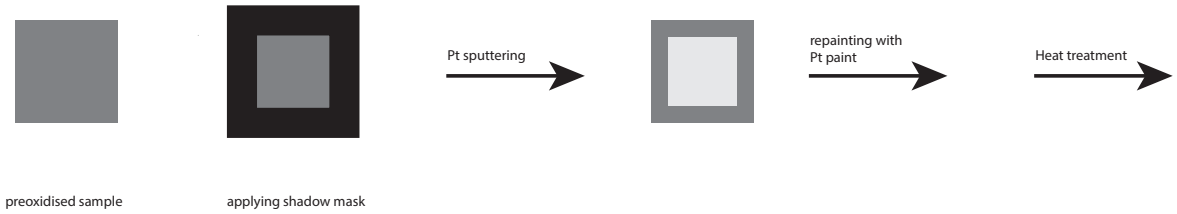

Figure 3.5: Scheme for electrode preparation.

was run at a frequency of 1 Hz, and each temperature was measured several times. Since the frequency was relatively low, the measurement was considered to be free from capacitive or inductive influences.

Chapter 4

Results and Discussion

4.1 Measurement validation

The chromium evaporation of the investigated substrate/coating combinations was measured by using the denuder technique. This unique technique allows the time resolved measurement of the volatilization of chromium. In order to check the reproducibility of the denuder technique, uncoated stainless steel 441 was exposed in different furnaces and at the same conditions; of 850 °C in 3 % water-containing air, which is plotted in Figure 4.1. Chromium evaporation was measured for almost 1200 h and over the entire exposure time it followed a linear trend. Two parallel exposures were done in different furnaces and after a total exposure time of about 1125 h the two runs deviated less than 1 %. In case of troubles in denuder handling or if samples were not standing correctly in the furnace, deviations in chromium evaporation were observed. Thus it was concluded that the method for measuring chromium evaporation was reliable as long as the samples were standing correctly in the holder and no handling errors were made. To ensure significant reliability, all further experiments were performed at least twice and whenever experimental problems were encountered the experiments were redone.

4.2 Stainless steel 441 as interconnect material

The first investigation was dedicated to the ferritic stainless steel AISI 441 which was coated with different nano coatings. AISI 441 was chosen as substrate material since it is available to a fraction of the price as comparable SOFC interconnect optimized ferritic steels.

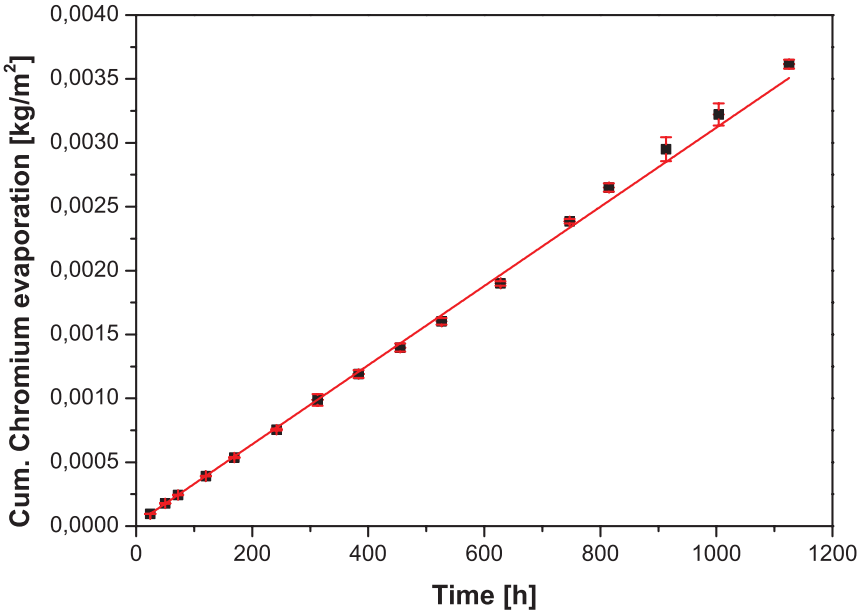

Figure 4.1: Chromium evaporation of uncoated 441.

4.2.1 Gravimetric measurements and Chromium evaporation

Both isothermal and discontinuous exposures were performed to monitor mass gain and chromium evaporation. The mass gain that was obtained by discontinuous exposures is plotted in Figure 4.2. After about 100 h of exposure, the uncoated material started to suffer from spallation and after 570 h a mass gain of 0.48 mg/cm^2 was observed. The cerium-coated material exhibited a mass gain of about 0.45 mg/cm^2 and the lanthanum-coated material of about 0.52 mg/cm^2 after a total exposure time of 570 h. The cerium/cobalt-coated material had a mass gain of 0.59 mg/cm^2 and the lanthanum/cobalt-coated material 0.58 mg/cm^2 after the same exposure time. Both of the RE/cobalt-coated samples had a mass gain of about 0.21 mg/cm^2 after only 100 min of exposure. All coated samples exhibited almost parabolic corrosion behavior after an initial oxidation of 100 min. The mass gain of the coated samples exposed discontinuously did not differ significantly from isothermally exposed samples. It was observed that the lanthanum/cobalt-coated samples were slightly bent after exposure.

In contrast to the discontinuous gravimetric exposures, the chromium evaporation was measured isothermally. The cummulated chromium evaporation over time is plotted in Figure 4.3. The uncoated material as well as the lanthanum-coated material exhibited similar chromium evaporation. The uncoated material evaporated a total mass of about 0.0014 kg/m^2 of chromium after 526 h of exposure. The lanthanum-coated material evaporated 0.0012 kg/m^2 chromium after 475 h of exposure time. The cerium-coated material evaporated 0.0015 kg/m^2 chromium during 500 h, which is about 10 % higher than the uncoated or lanthanum-coated material.

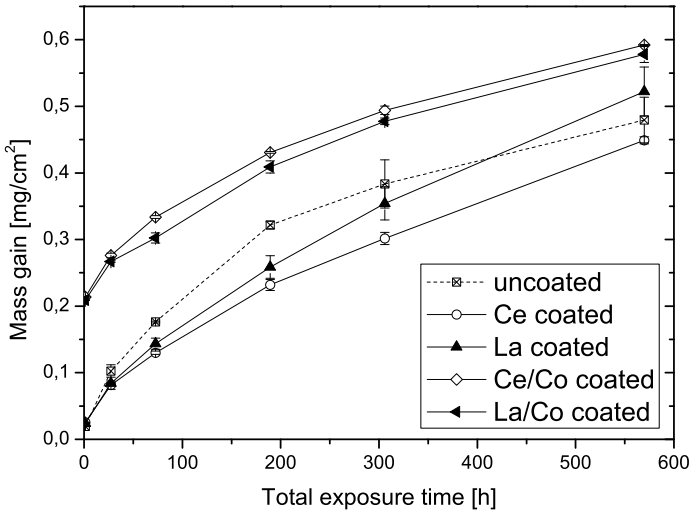

Figure 4.2: Mass gain of stainless steel 441 with different coatings.

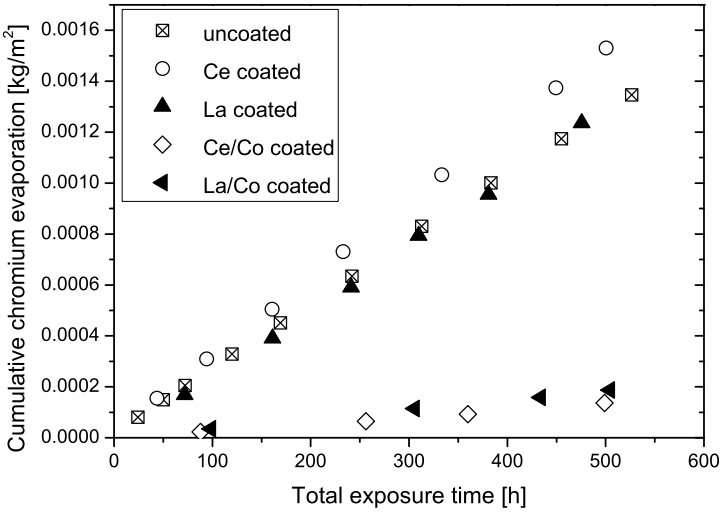

Figure 4.3: Chromium evaporation of stainless steel 441 with different coatings.

The cerium/cobalt-coated material showed a reduction of about 10 times in chromium evaporation and evaporated about 0.00014 kg/m^2. The lanthanum/cobalt-coated material evaporated also approximately 10 times less chromium than the uncoated material, with about 0.00019 kg/m^2 after about 500 h of exposure time.

The chromium evaporation, as shown in Figure 4.3, followed almost a linear trend.

A slight decrease in the evaporation rate was seen after the first few measurements. For this observation one might assume an initial oxidation towards a double-layered oxide scale. The evaporation decreased after a continuous outer manganese spinel oxide layer had formed. Comparing the chromium volatilization of the cerium-coated with the lanthanum-coated material, the 10 % increase in chromium evaporation led to the conclusion that the chromium evaporation was increased by cerium. One might suspect either a catalytic effect of cerium, due to its two oxidation states, or since it is known to suppress outward metal ion diffusion, a simply thinner outer oxide layer. The latter theory might be supported by the microstructural observation in section 4.2.2. The RE/cobalt-coated samples also showed a linear trend in chromium evaporation. The very quick initial oxidation of the cobalt top coating to Co_3O_4 led to immediate protection against chromium evaporation and acts as a cap layer. The outward diffusion of manganese might improve retention even further.

Mass gain is one of the main tools for predicting the lifetime of an oxidizing steel. In the present investigation two complications occurred in comparing the different coating systems; the constant chromium evaporation led to a mass loss and in case of the cobalt top coatings, an initial mass gain was obtained. Therefore the mass gain data was combined with the chromium evaporation data to better compare the different coating systems. The evaporated chromium was added to the mass gain by assuming that every mg of lost chromium is equal to 1.46 mg of Cr_2O_3 in the oxide scale. Additionally, the initial oxidation of the cobalt top coating was subtracted from the cobalt-coated samples, by calculating the theoretical mass gain for a 630 nm thick cobalt coating oxidized to Co_3O_4, which is equal to 0.202 mg/cm^2. The aim was to obtain a clearer picture of the influence of the different coatings on the corrosion properties. The recalculated mass gain is plotted in Figure 4.4. Due to the massive spallation observed on the uncoated material, and therefore the large difference between isothermal and discontinuous exposure, the uncoated material was excluded from the plot. The updated plot clearly shows not only the beneficial effect of the reactive element coatings, but also the positive effect the cobalt top coating had on corrosion performance. The highest compensated mass gain was obtained with the lanthanum-coated samples, whereas the cerium-coated material oxidized slightly slower. The most distinctive revealed effect of this plot is the positive influence of the cobalt top coating. In previous studies on Sandviks Sanergy HT only a very small negligible effect of the cobalt top coating on the oxidation properties was observed [47]. In a different investigation in contrast, by Yang et al. reported a beneficial effect of a $Mn_{1.5}Co_{1.5}O_4$ coating on AISI 441 [48]. Their interpretation of this observation was a limited oxygen inward diffusion, which might be supported by this study.

4.2.2 Microstructural evolution

Several SEM analysis were done on the exposed samples to obtain a better understanding of the underlying oxidation processes. A top-view image of an uncoated

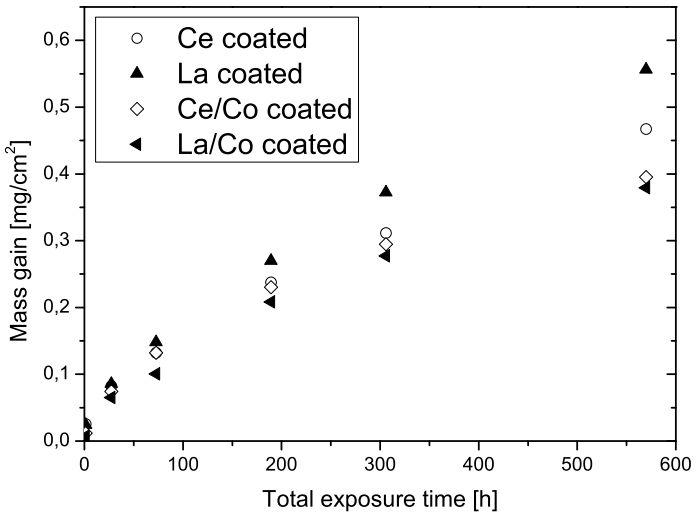

Figure 4.4: Compensated mass gain of stainless steel 441 with different coatings.

sample is depicted in Figure 4.5. The surface of the uncoated material appeared relatively buckled, with a linear texture, and at several locations, spallation was observed. The spallation was also observable by visual inspection and occurred for exposure times longer than 100 h. The cross-section of the same material, see Figure 4.6, showed a double-layered oxide, with a relatively thin (approx. 0.8 μm) outer oxide and thicker (approx 3.6 μm thickness) inner oxide. An EDX analysis, shown in Figure 4.7, proved the presence of an outer manganese-rich oxide with a chromium-rich inner oxide. A zone of internal titanium rich oxide was observed beneath the double layer oxide. Additionally, some Laves phases located in grain boundaries, mainly containing niobium and silicon, could be seen.

The observed amount of spallation during this study was relatively high compared to similar studies reported in literature. Liu et al. have reported on a small amount of spallation for uncoated AISI 441 when exposed in stagnant air. Even though it is questionable if their investigated steel had a different chemical composition or due to their experimental conditions less thermal stresses were present [49]. The observations of Yang et al. are in line with Liu's observation who reports spallation to a lesser extent and also at longer exposure times [48]. One might suspect Yang's observation could have been caused by the lower exposure temperature of about 800 °C. A common suggestion for oxide scale spallation in this context is a sub-scale silica formation [8]. This was initially supported by the observations of Jablonski et al. who concluded that niobium content as well as high exposure temperatures do not allow for the complete capture of the silicon contained in the steel [12]. Additionally, the investigated batch of AISI 441 contained a relatively large amount of silicon (0.55

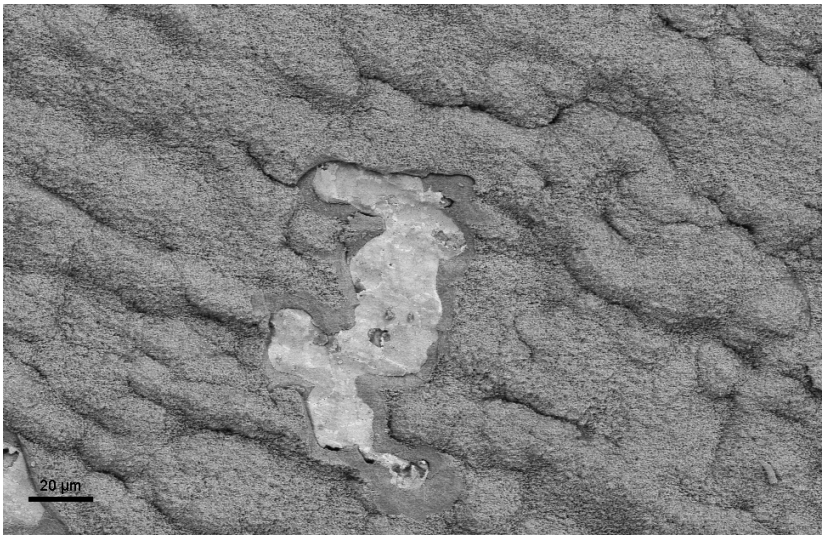

Figure 4.5: Topview of an uncoated sample exposed for 500 h.

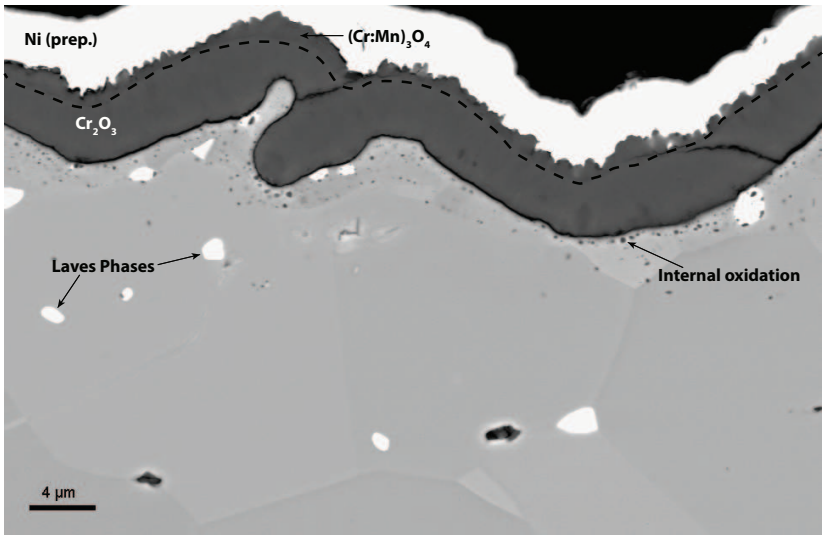

Figure 4.6: Cross-section of an uncoated sample exposed for 500 h.

wt.% compared to 0.33 wt.%) compared to Jablonski's investigation.
In contrast to the uncoated samples, no spallation was observed on the cerium- and the lanthanum-coated material (Figures 4.8 and 4.11). Nevertheless, a linear texture within the buckling was clearly visible. The cross-section of a cerium-coated sample confirmed, once again, a double-layered oxide, see Figure 4.9. Although the thickness was slightly thinner (outer oxide approx. 0.5 μm and inner oxide approx. 2.3 μm). The EDX analysis did not differ significantly from the uncoated material, as shown in Figure 4.10. Again a zone of internal oxidation with titanium oxides and niobium and silicon rich Laves phases could be observed.

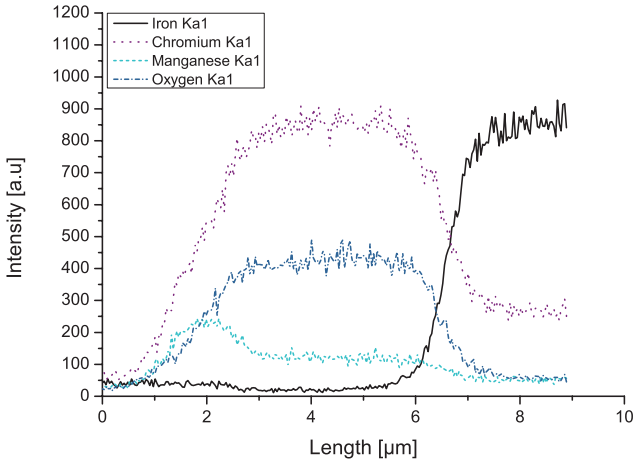

Figure 4.7: EDX line scan of an uncoated sample cross-section exposed for 500 h.

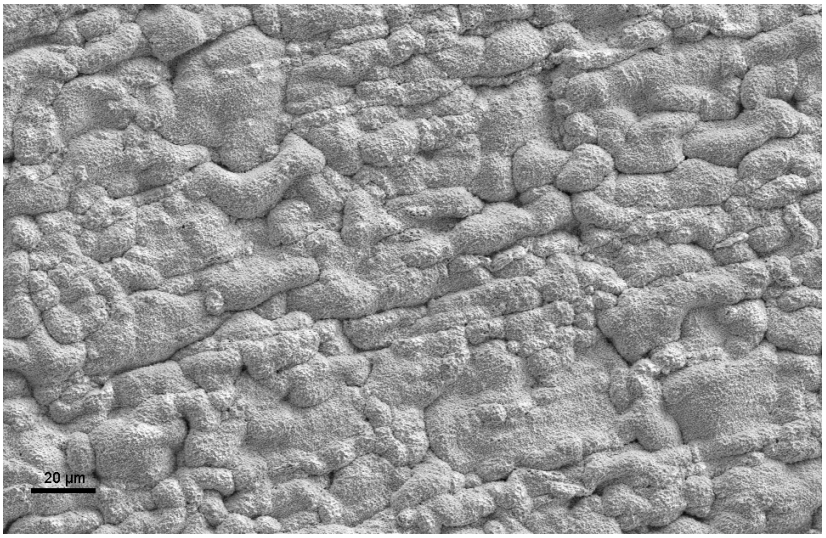

Figure 4.8: Topview of a cerium-coated sample exposed for 500 h.

A structure similar to the one seen for the cerium-coated material was observed in the cross-section of the lanthanum-coated material, plotted in Figure 4.12. The thicknesses of the two oxide layers were with 0.8 μm for the outer and 2.1 μm in a comparable range. The EDX analysis did not reveal any major differences (see Figure 4.13.

To investigate whether or not subscale silica formation causes the severe spallation observed in the uncoated material, two FIB cross-sections; one of an uncoated sample and one of a cerium-coated sample, were prepared. This was done in order to exclude any potential contamination caused by the polishing process. Figure 4.14 shows an EDX line scan of the uncoated sample and Figure 4.15 shows the same for the cerium-coated sample. It can be seen, that in both cases a subscale silica layer has

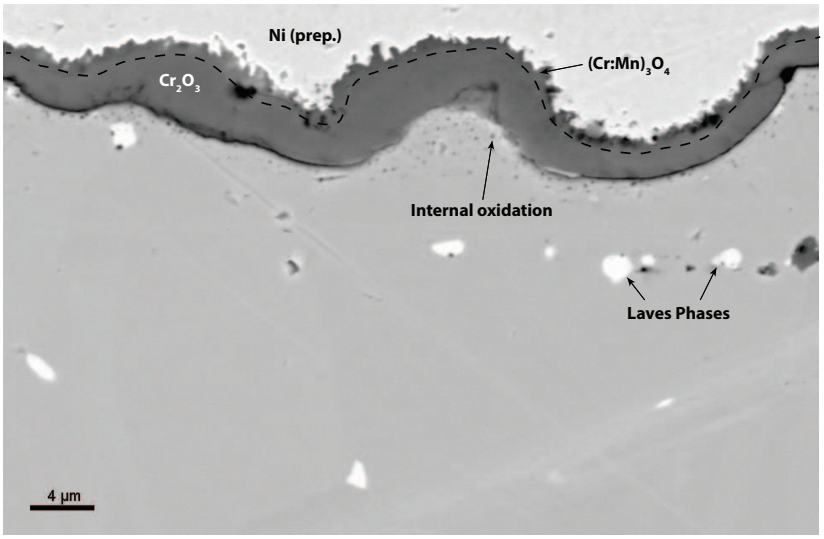

Figure 4.9: Cross-section of a cerium-coated sample exposed for 500 h.

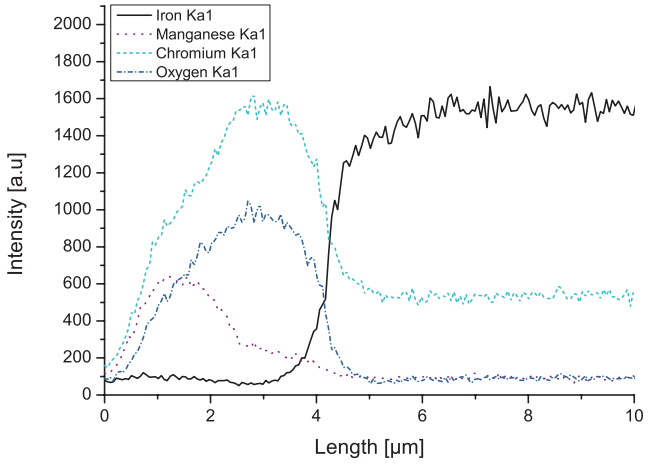

Figure 4.10: EDX line scan of a cerium-coated sample cross-section exposed for 500 h.

been formed. Thus it can be concluded that the findings of Jablonski et al., concerning sub-scale silica formation being caused by insufficient silicon capture in the Laves phases, are confirmed. Questionable in this context is whether or not subscale silica formation solely causes scale spallation. Both reactive element coatings improved the scale adhesion successfully. Even though the exposure temperatures for observing a reactive element effect are relatively low, these observations are in line with other studies [50, 51]. Several researchers have proposed mechanisms for this beneficial effect; such as a reduction in growth rate, a higher scale plasticity, a reduction in growth stress or an improved scale-alloy interface [52, 53]. Based on the investigations made, it must be concluded that the observed spallation cannot be solely caused by sub-scale silica formation. A beneficial effect of the cerium coating in preventing silica subscale formation, as seen by Alman et al. could not be confirmed [23]. One might suspect

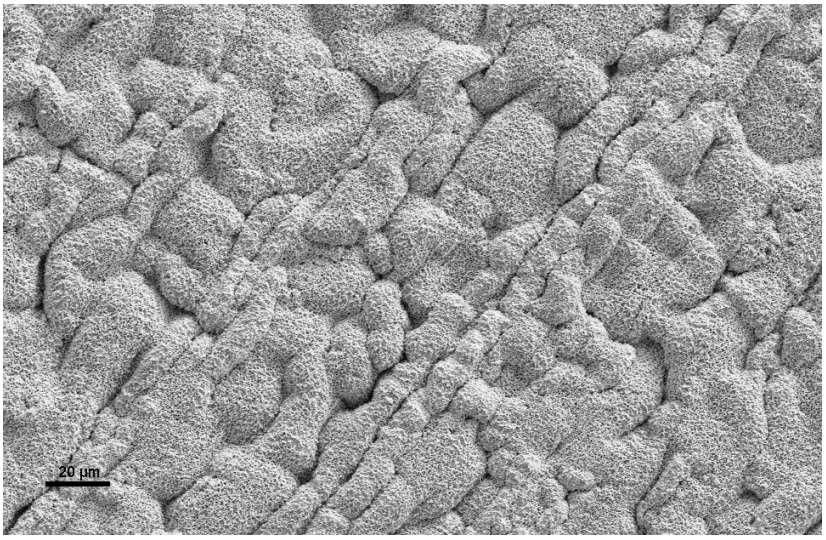

Figure 4.11: Topview of a lanthanum-coated sample exposed for 500 h.

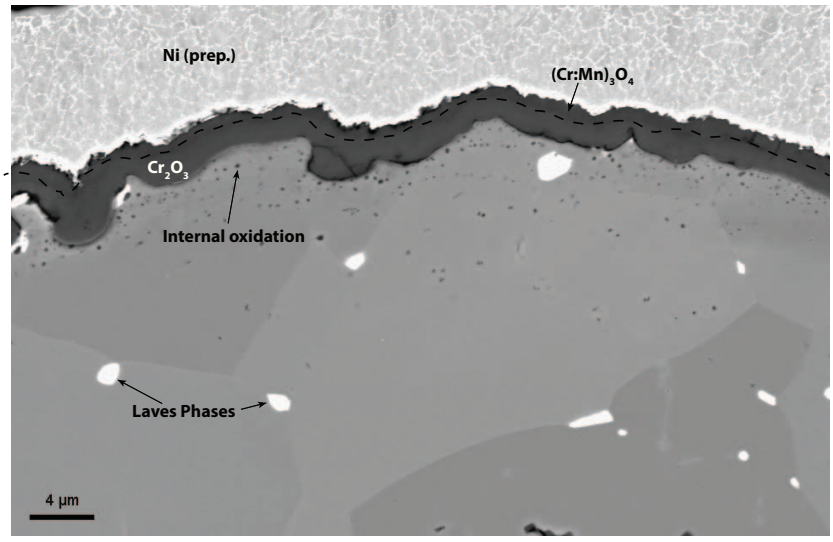

Figure 4.12: Cross-section of a lanthanum-coated sample exposed for 500 h.

a combination a weakened scale adhesion, caused by silica formation and occurring growth stresses that in both cause the scale spallation. The growth stresses can be decreased by reactive element coatings which then prevent scale spallation.

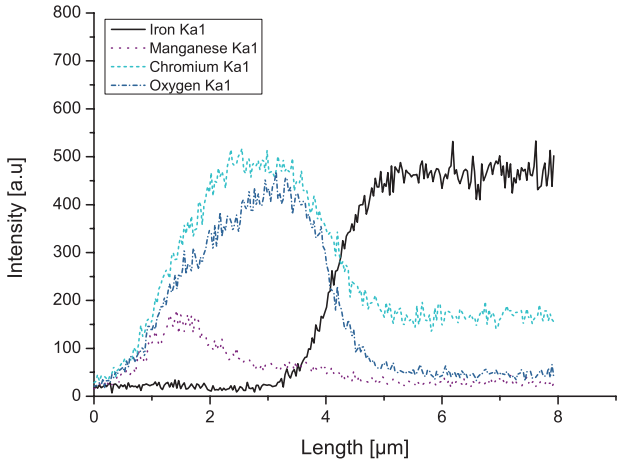

Figure 4.13: EDX line scan of a lanthanum-coated sample cross-section exposed for 500 h.

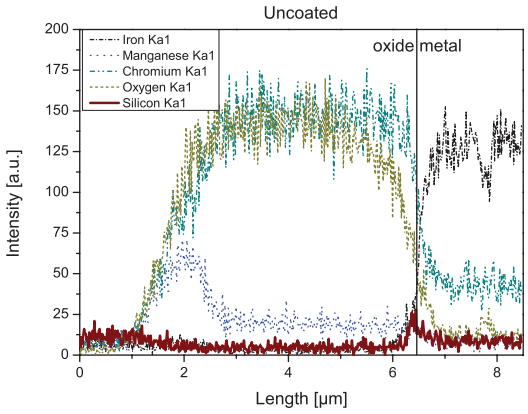

Figure 4.14: EDX line scan of a FIB-prepared uncoated sample exposed for 500 h.

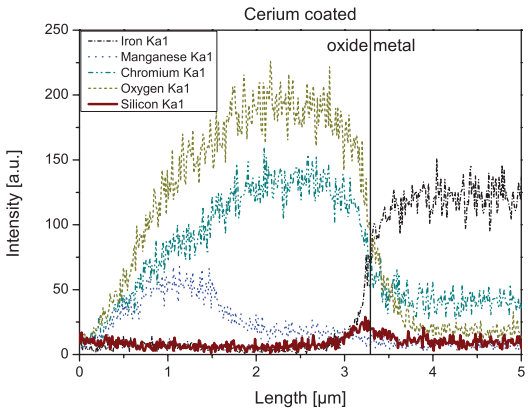

Figure 4.15: EDX line scan of a FIB prepared cerium-coated sample exposed for 500 h.

In contrast to the uncoated and the reactive-element-coated materials appeared the surface on the cerium/cobalt coated samples, as one is shown in Figure 4.16, to be much smoother. The smoothening effect was also seen in the cross-sectional micrograph (see Figure 4.17). The observed double-layer oxide appeared, due to the cobalt top coating, much thicker in the outer oxide layer with about 1.9 μm and relatively thin with 1.4 μm in inner oxide layer. The outer oxide layer is rich in cobalt and manganese whereas the inner oxide layer is mostly composed of chromium oxide, as the EDX line scan shows, plotted in Figure 4.18. Once again, internal oxidation and Laves phases, as in the previous cases, were observed. The observed smoother surface is assumed to be a result of the cobalt top coating, which was deposited as metal. The large volume expansion leads to an evening out of the linear texture.

An explanation for the texture only being present on the uncoated and RE-coated sample surfaces could be the rolling marks present in the steel prior to exposure induced during production.

Figure 4.16: Topview of a cerium/cobalt-coated sample exposed for 500 h.

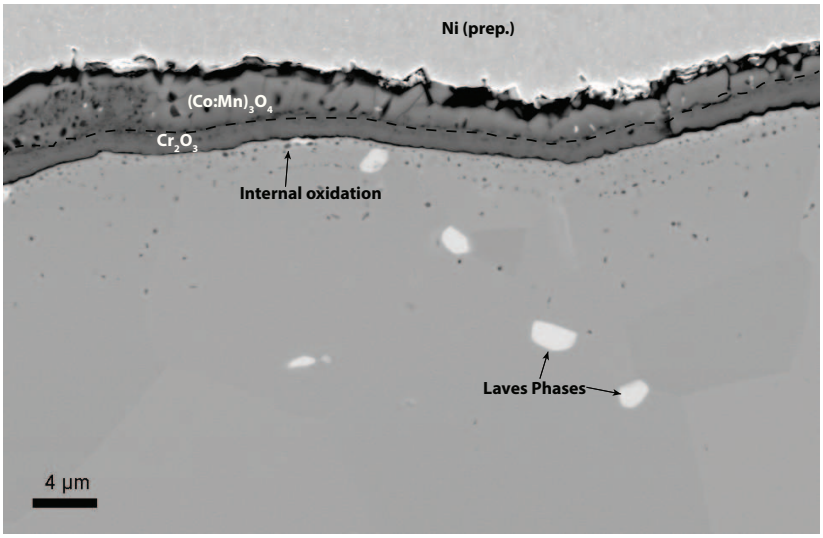

Figure 4.17: Cross-section of a cerium/cobalt-coated sample exposed for 500 h.

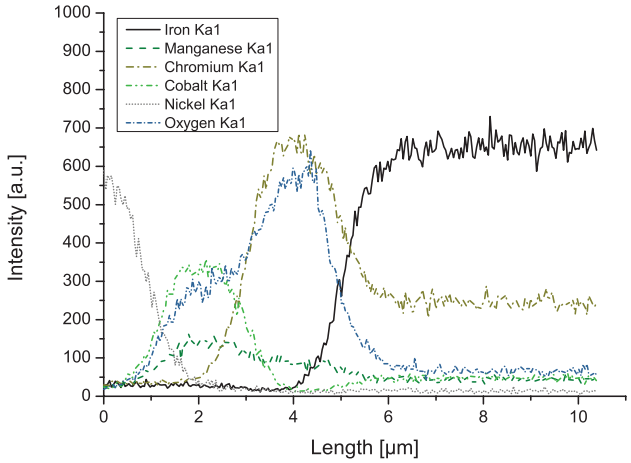

Figure 4.18: EDX line scan of a cerium/cobalt-coated sample cross-section exposed for 500 h.

The surface of a lanthanum/cobalt-coated sample is shown in Figure 4.19. It can be seen that the surface is slightly more wavy than the cerium/cobalt-coated material. The cross-section (see Figure 4.20) confirmed the increase in waviness. An EDX line scan, depicted in Figure 4.21, did in not show any major compositional differences to the cerium/cobalt-coated sample. The increased waviness might be caused by the large bending observed after removal from the furnace.

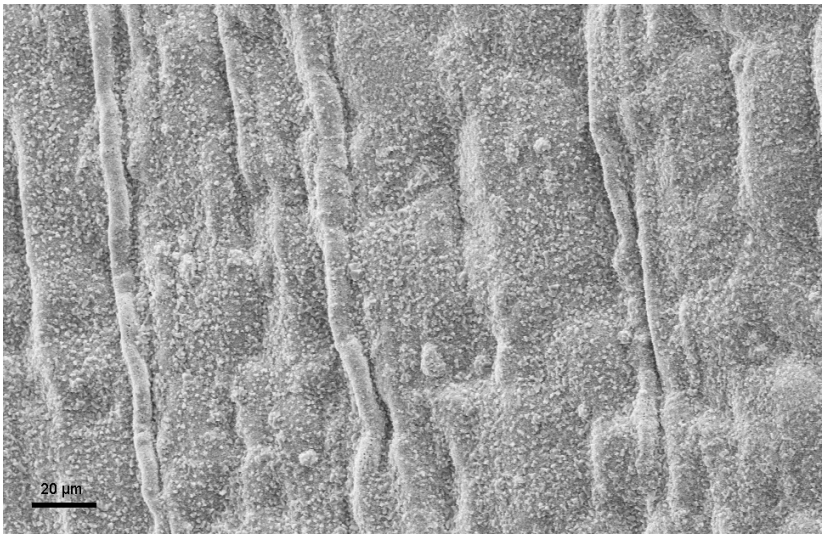

Figure 4.19: Topview of a lanthanum/cobalt-coated sample exposed for 500 h.

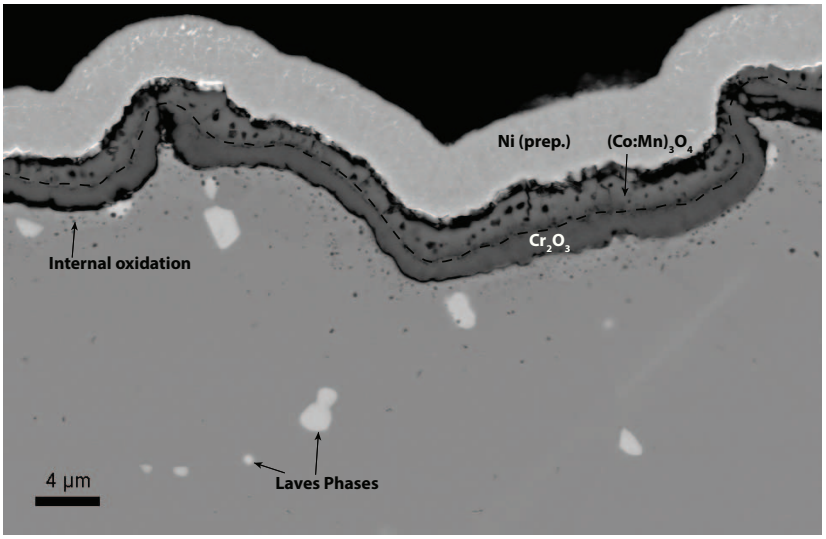

Figure 4.20: Cross-section of a lanthanum/cobalt-coated sample exposed for 500 h.

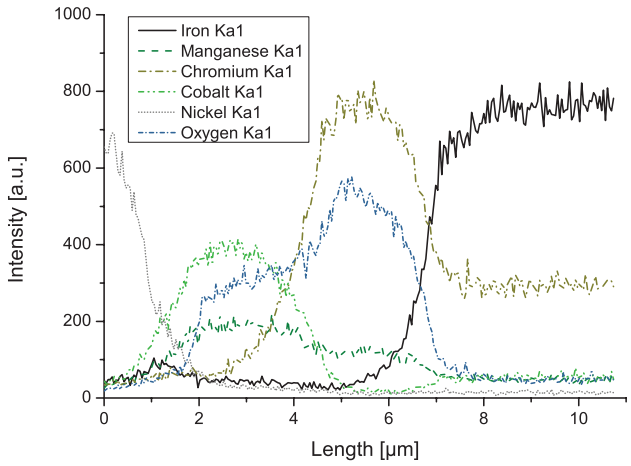

Figure 4.21: EDX line scan of a lanthanum/cobalt-coated sample cross-section exposed for 500 h.

4.3 Copper based conversion coatings

The second investigation was aimed to investigate Sandvik Sanergy HT coated with copper/manganese and copper/iron spinel forming coatings in a cathode atmosphere. These coatings were chosen because of the lower material price of copper compared to cobalt and the higher theoretical electrical conductivity of copper spinels.

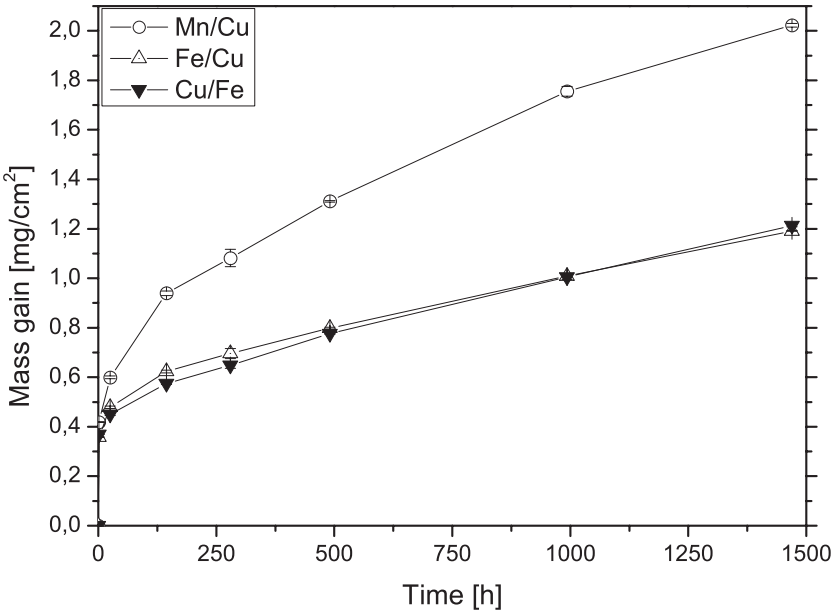

Figure 4.22: Mass gain of stainless steel Sandvik Sanergy HT with different copper conversion coatings.

4.3.1 Mass gain

The mass gain was measured during discontinuous exposures at intervals with increasing duration. The mass gain for 1500 h exposure time is plotted in Figure 4.22. Both copper/iron coatings performed relatively similarly with a mass gain of 1.2 mg/cm^2 after being exposed for almost 1500 h. The manganese/copper-coated material gained substantial more mass and reached a value of 2.0 mg/cm^2 after the same exposure time. Compared to previous results at HTC [47] for cobalt-coated Sandvik Sanergy HT, which gained approx. 1.5 mg/cm^2 after 1500 h exposure time, the copper/iron coatings were significantly lower in mass gain, while the manganese/copper coating was well above that value.

4.3.2 Chromium evaporation

The chromium evaporation of the manganese/copper-coated and the iron/copper-coated material was measured for 500 h, while the copper/iron-coated material was measured for 1000 h. The chromium evaporation is shown in Figure 4.23. The manganese/copper-coated material evaporated a total mass of 0.0012 kg/m^2 after an exposure time of 500 h, and the iron/copper-coated material evaporated approximately 0.0005 kg/m^2 after 500 h. The copper/iron-coated material released a mass of 0.00028 kg/m^2 after 500 h and after the total exposure time of 1000 h, a cummulated evaporation of 0.00067 kg/m^2 was reached. Compared to uncoated Sandvik Sanergy HT [47] it is obvious that the manganese/copper coating had almost no effect on the chromium evaporation, while the iron/copper coating decreases the chromium evap-

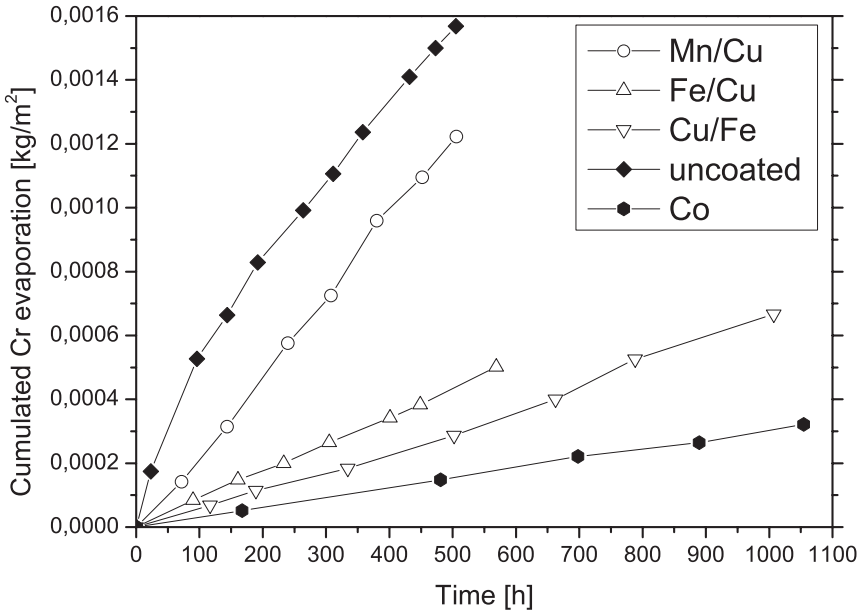

Figure 4.23: Chromium evaporation of stainless steel Sandvik Sanergy HT with different copper conversion coatings, compared to uncoated and cobalt-coated [47].

oration with about 50-70 %, and the copper/iron coated material reduces chromium evaporation about 80 %. Compared to cobalt coatings, which decreased chromium evaporation about 90 % the copper/iron coating seemed to be almost as effective in chromium retention.

4.3.3 Microstructural evolution

After exposing the samples continuously for 500 h, a microstructural investigation was done. The samples were prepared using epoxy embedding, and prior to preparation a protective nickel coating was applied. The cross-sectional micrograph of a manganese/copper-coated sample with a corresponding EDX line scan is shown in Figures 4.24 and 4.25. The total oxide thickness of the double-layered oxide was about 10 μm. The oxide scale was detached at several locations and pores were observed at the metal/oxide interface. The outer oxide layer consisted mainly of copper and manganese with relatively high amounts of chromium, whereas the inner oxide layer contained mainly chromium oxide.
The manganese/copper-coated samples did not show improved properties in terms of chromium evaporation and corrosion. The coating was not considered to be beneficial for the interconnect performance at 850 °C. This observation is in line with the findings of Wei et al. who have investigated similar coatings of manganese and copper on UNS 430 at different temperatures [54]. They observed, as in the present study, pores within the oxide scale and concluded a maximum operation temperature of about 750 °C. The substrate suffered in their study at temperatures of 850 °C and above from corrosion, while below that temperature almost no chromia below

the coating was formed. This could be an explanation for the, in our case observed, relatively high chromium evaporation due to a breakdown of the protective scale. In an earlier study Paulson et al. have mentioned the diffusion of iron and chromium through copper manganese coatings [55]. In this study, a different ratio between copper and manganese compared to Paulson et al. also could be a reason for the observation of the relatively high corrosion [55]. The manganese copper coating might be more effective in mitigating chromium volatilization at lower operational temperatures, however at the investigated temperature it was not effective.

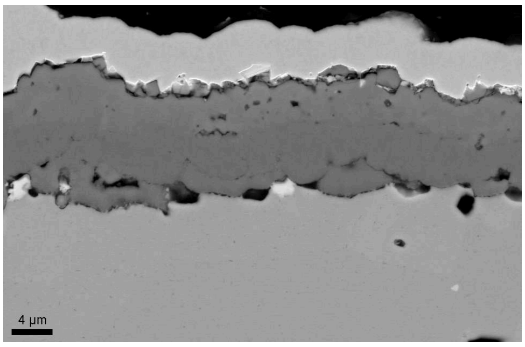

Figure 4.24: Cross-sectional SEM micrograph of a manganese/copper-coated sample exposed for 500 h.

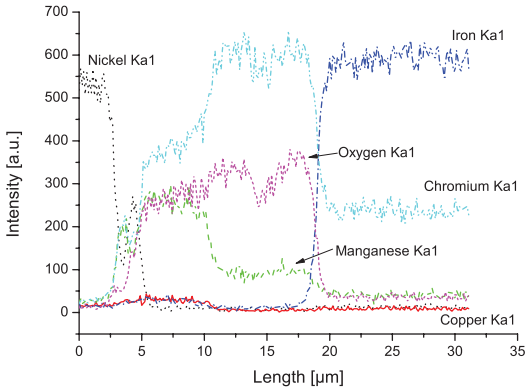

Figure 4.25: EDX line scan of a manganese/copper-coated sample exposed for 500 h.

The cross-section of a iron/copper-coated sample, shown in Figure 4.26, reveals a stronger contrast in the double-layer oxide. With a total oxide thickness of about 5 μm, the oxide was about 50 % thinner than the manganese/copper-coated samples. Additionally a well adhered oxide scale was present over the entire sample surface and almost no pores at the metal/oxide interface were observed. The EDX line scan analysis (see Figure 4.27) showed an outer oxide layer consisting of mainly copper and iron with chromium and some manganese, whereas the inner oxide layer mainly contained chromium oxide with a small fraction of manganese.

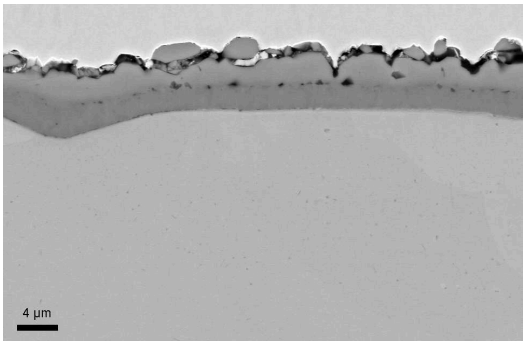

Figure 4.26: Cross-sectional SEM micrograph of a iron/copper coated sample exposed for 500 h.

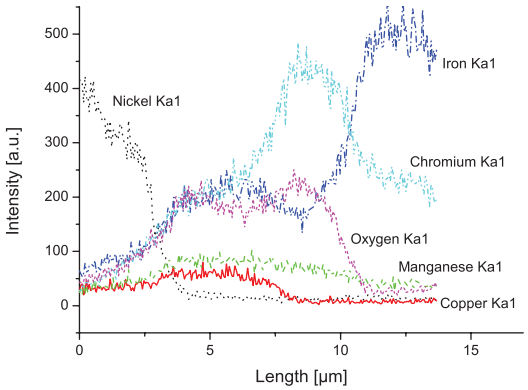

Figure 4.27: EDX line scan of a iron/copper coated sample exposed for 500 h.

Similar to the iron/copper coated material, the copper/iron-coated material also showed a well adhered oxide scale, as it can be seen in Figure 4.28. In this case a double-layered oxide layer of about 5 μm thickness was also observed. Only very small pores could be seen at the oxide layer interface. The corresponding EDX analysis confirmed that the outer oxide was consisting mainly of iron and copper with an outwards decreasing manganese and chromium content and is plotted in Figure 4.29. The peak of iron was shifted slightly more outwards than the copper peak, in contrast to the previous case. The inner oxide mainly consisted of chromium oxide with a small amount of manganese.

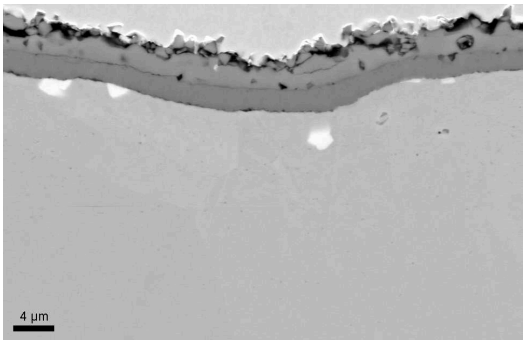

Figure 4.28: Cross-sectional SEM micrograph of a copper/iron-coated sample exposed for 500 h.

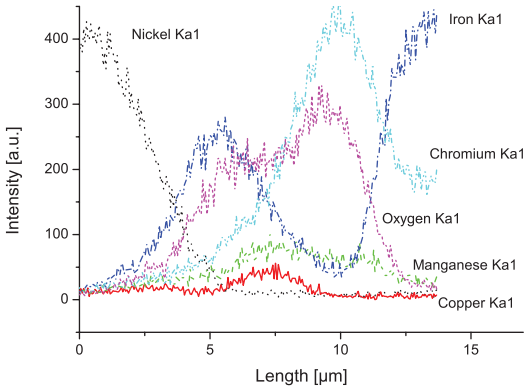

Figure 4.29: EDX line scan of a copper/iron-coated sample exposed for 500 h.

Both iron and copper-containing coatings showed relatively similar properties, both in mass gain, evaporation and microstructural evolution. A slight advantage at longer exposure times was observed in mass gain compared to the cobalt coating [47]. In this context it is important to mention that the coating thickness for all copper con-

version coatings was not yet optimized. One might suspect better performance when the thickness is optimized.

4.4 Electrical properties

The highest performances in chromium evaporation and corrosion properties were obtained with the cobalt/cerium coated stainless steel 441 in the first investigation. This substrate/coating system was consequently selected for an electrical characterization. The Area Specific Resistance (ASR), including mass gain, curve for the cobalt/cerium-coated 441 is shown in Figure 4.30, the plot represents the ASR measured at 850 °C for different pre-oxidation times. It can be seen that both the the mass gain and the ASR follow a similar trend over the entire exposure time.

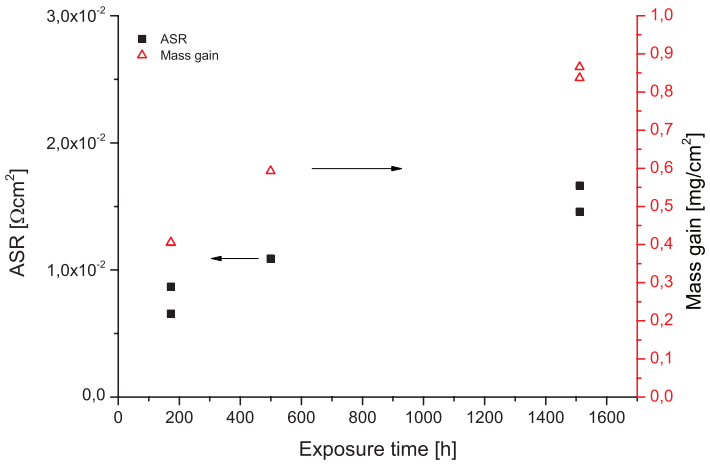

Figure 4.30: ASR and mass gain for cerium/cobalt-coated AISI 441 versus time, measured at 850 °C.

The resistance was measured at several temperatures in order to ensure that the main contribution to the resistance value is determined by the oxide. A cool down curve for a 1500 h exposed sample is shown in Figure 4.31, that cool-down curve was then transferred into an Arrhenius plot to calculate an activation energy, see Figure 4.32. The temperature dependence of the measured resistance clearly shows a semi-conducting behaviour, that can be related to the oxide scale. The calculated activation energy was about 0.6 eV. Compared to literature values this is well within the region of other cobalt-coated ferritic stainless steels, Molin et al. has measured an activation energy of about 0.75 eV for cobalt-coated Crofer 22 APU exposed for more than 500 h [56]. Since the theoretical value for $MnCo_2O_4$ is about 0.55 eV, one might assume that the electrical conductivity is significantly influenced by the cobalt top coating [36]. In contrast, activation energies for thermally grown oxides

for other uncoated ferritic stainless steels are in the range of 0.8 - 1 eV [39, 57]. Further experiments with samples pre-exposed for longer times; preferably cerium-coated samples, seem to be necessary to prove this assumption.

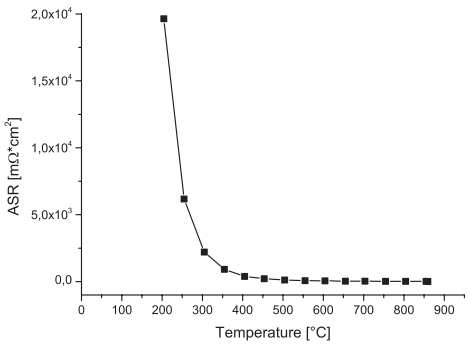

Figure 4.31: ASR values measured on a cerium/cobalt-coated AISI 441 sample exposed for 1500 h.

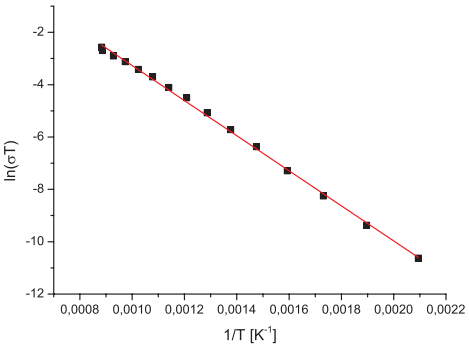

Figure 4.32: Arrhenius plot of ASR values measured on a cerium/cobalt-coated AISI 441 sample exposed for 1500 h.

Chapter 5

Summary and Outlook

The findings during this research can be concluded as follows: The denuder technique was proven to be very effective in measuring the volatilization of chromium. Over long exposure times with uncoated AISI 441 standard deviations less than 1 % were observed and high reproducibility was ensured during all measurements.

The investigation on coated AISI 441 in a cathode atmosphere lead to the conclusion that AISI 441 coated with cerium/cobalt is as effective as comparable commercially available SOFC steels. Reactive-element coatings improve the scale adhesion and corrosion resistance, but do not have a positive effect on decreasing chromium volatilization. Lanthanum/cobalt-coated 441 samples were not as promising as cerium/cobalt-coated samples due to less mechanical stability. Further experiments should be focused on longer exposure times for cerium/cobalt-coated AISI 441 combined with an electrical characterization. Anode side exposures should be performed and suitable anode side coatings be developed.

Copper-based conversion coatings on Sandvik Sanergy HT can prevent chromium evaporation successfully. While the manganese/copper coating proved not to be beneficial at the investigated temperature in terms of mass gain and chromium evaporation, showed both iron- and copper-containing coatings a good potential to function as a cathode side coating.

A method for ASR characterization was developed. The challenge in obtaining reasonable ASR data was to find a way to contact the oxide scale to the measurement equipment. The suggested way of electrode preparation led to electrodes with an almost similar area and a low sheet resistance. Since the measured resistance increased with exposure time similar to the mass gain curve and the resistance was proving to have a semiconducting temperature dependence, it was assumed that the obtained data was reliable.

Future research will be aimed at electrical characterization of the already investigated substrate/coating combinations, since some of the investigated substrate/coating combinations were promising in corrosion and chromium evaporation. In this context especially the copper/iron coatings seem promising, due to their low theoretical electrical resistance.
Lower exposure temperatures, potentially combined with a technically relevant priming step before, could also be of interest. Furthermore a combination of reactive-element-coated 441 with copper-conversion coatings seem to be promising. Besides the already investigated substrate/coating combinations, interactions between SOFC electrode materials as wells as sealing materials should be performed, too.

References

[1] P.-F Nagel. *Electricity from wood through the combination of gasification and solid oxide fuel cells*. PhD thesis, ETH Zurich, 2008.

[2] S. M. Haile. Fuel cell materials and components. *Acta Materialia*, 51(19):5981–6000, 2003.

[3] R. M. Ormerod. Solid oxide fuel cells. *Chemical Society Reviews*, 32(1):17–28, 2003.

[4] N. Q. Minh. Ceramic fuel-cells. *Journal of the American Ceramic Society*, 76(3):563–588, 1993.

[5] R. Pornprasertsuk, P. Ramanarayanan, C. B. Musgrave, and F. B. Prinz. Predicting ionic conductivity of solid oxide fuel cell electrolyte from first principles. *Journal of Applied Physics*, 98(10), 2005.

[6] S. C. Singhal. Advances in solid oxide fuel cell technology. *Solid State Ionics*, 135(1-4):305–313, 2000.

[7] J. W. Fergus. Metallic interconnects for solid oxide fuel cells. *Materials Science and Engineering a-Structural Materials Properties Microstructure and Processing*, 397(1-2):271–283, 2005.

[8] W. J. Quadakkers, J. Piron-Abellan, V. Shemet, and L. Singheiser. Metallic interconnectors for solid oxide fuel cells - a review. *Materials at High Temperatures*, 20(2):115–127, 2003.

[9] S. Linderoth, P. V. Hendriksen, M. Mogensen, and N. Langvad. Investigations of metallic alloys for use as interconnects in solid oxide fuel cell stacks. *Journal of Materials Science*, 31(19):5077–5082, 1996.

[10] H. Y. Tu and U. Stimming. Advances, aging mechanisms and lifetime in solid-oxide fuel cells. *Journal of Power Sources*, 127(1-2):284–293, 2004.

[11] J. W. Fergus. Lanthanum chromite-based materials for solid oxide fuel cell interconnects. *Solid State Ionics*, 171(1-2):1–15, 2004.

[12] P. D. Jablonski, C. J. Cowen, and J. S. Sears. Exploration of alloy 441 chemistry for solid oxide fuel cell interconnect application. *Journal of Power Sources*, 195(3):813–820, 2010.

[13] M. Stanislowski, E. Wessel, K. Hilpert, T. Markus, and L. Singheiser. Chromium vaporization from high-temperature alloys i. chromia-forming steels and the influence of outer oxide layers. *Journal of the Electrochemical Society*, 154(4):A295–A306, 2007.

[14] R.N. Sachitanand. Evaluation of the oxidation and cr evaporation properties of selected fecr alloys used as sofc interconnects. *International Journal of Hydrogen Energy*, submitted, 2013.

[15] Per Kofstad. *High Temperature Corrosion*. Elsevier Applied Science, 1988.

[16] Michael Schütze. *Protective Oxide Scales and Their Breakdown*. John Wiley & Sons, 1997.

[17] H.J.T. Ellingham. Reducibility of oxides and sulfides in metallurgical processes. *Journal of the Society of Chemical Industry*, 63:125, 1944.

[18] http://oregonstate.edu/instruct/me581/homework/overheads/ellingham.jpg.

[19] Niklas Israelsson. High temperature corrosion of fecral alloys, 2013.

[20] C. Wagner. The theory of the warm-up process. *Zeitschrift Fur Physikalische Chemie-Abteilung B-Chemie Der Elementarprozesse Aufbau Der Materie*, 21(1/2):25–41, 1933.

[21] N. Bricks, G. H. Meier, and Pettit F. S. *Introduction to the High-Temperature Oxidation of Metals*. Cambridge University Press, 2009.

[22] P. Huczkowski, N. Christiansen, V. Shemet, J. Pironabellan, L. Singheiser, and W. J. Quadakkers. Oxidation limited life times of chromia forming ferritic steels. *Materials and Corrosion-Werkstoffe Und Korrosion*, 55(11):825–830, 2004.

[23] D. E. Alman and P. D. Jablonski. Effect of minor elements and a ce surface treatment on the oxidation behavior of an fe-22cr-0.5mn (crofer 22 apu) ferritic stainless steel. *International Journal of Hydrogen Energy*, 32(16):3743–3753, 2007.

[24] B. A. Pint. Progress in understanding the reactive element effect since the whittle and stringer literature review.

[25] D. P. Whittle and J. Stringer. Improvements in high-temperature oxidation resistance by additions of reactive elements or oxide dispersions. *Philosophical Transactions of the Royal Society of London Series a-Mathematical Physical and Engineering Sciences*, 295(1413):309–&, 1980.

[26] S. Fontana, R. Amendola, S. Chevalier, P. Piccardo, G. Caboche, M. Viviani, R. Molins, and M. Sennour. Metallic interconnects for sofc: Characterisation of corrosion resistance and conductivity evaluation at operating temperature of differently coated alloys. *Journal of Power Sources*, 171(2):652–662, 2007.

[27] S. Chevalier, C. Valot, G. Bonnet, J. C. Colson, and J. P. Larpin. The reactive element effect on thermally grown chromia scale residual stress. *Materials Science and Engineering a-Structural Materials Properties Microstructure and Processing*, 343(1-2):257–264, 2003.

[28] W. Qu, L. Jian, D. G. Ivey, and J. M. Hill. Yttrium, cobalt and yttrium/cobalt oxide coatings on ferritic stainless steels for sofc interconnects. *Journal of Power Sources*, 157(1):335–350, 2006.

[29] B. B. Ebbinghaus. Thermodynamics of gas-phase chromium species - the chromium oxides, the chromium oxyhydroxides, and volatility calculations in waste incineration processes. *Combustion and Flame*, 93(1-2):119–137, 1993.

[30] B. B. Ebbinghaus. Thermodynamics of gas-phase chromium species - the chromium chlorides, oxychlorides, fluorides, oxyfluorides, hydroxides, oxyhydroxides, mixed oxyfluorochlorohydroxides, and volatility calculations in waste incineration processes. *Combustion and Flame*, 101(3):311–338, 1995.

[31] M. Stanislowski, J. Froitzheim, L. Niewolak, W. J. Quadakkers, K. Hilpert, T. Markus, and L. Singheiser. Reduction of chromium vaporization from sofc interconnectors by highly effective coatings. *Journal of Power Sources*, 164(2):578–589, 2007.

[32] H. Kurokawa, C. P. Jacobson, L. C. DeJonghe, and S. J. Visco. Chromium vaporization of bare and of coated iron-chromium alloys at 1073 k. *Solid State Ionics*, 178(3-4):287–296, 2007.

[33] K. Huang, P. Y. Hou, and J. B. Goodenough. Reduced area specific resistance for iron-based metallic interconnects by surface oxide coatings. *Materials Research Bulletin*, 36(1-2):81–95, 2001.

[34] J. Froitzheim and J. E. Svensson. *Multifunctional Nano-Coatings for SOFC Interconnects*, volume 35 of *ECS Transactions*, pages 2503–2508. 2011.

[35] S. Canovic, J. Froitzheim, R. Sachitanand, M. Nikumaa, M. Halvarsson, L. G. Johansson, and J. E. Svensson. Oxidation of co- and ce-nanocoated fecr steels: A microstructural investigation. *Surface and Coatings Technology*, 215(0):62–74, 2013.

[36] A. Petric and H. Ling. Electrical conductivity and thermal expansion of spinels at elevated temperatures. *Journal of the American Ceramic Society*, 90(5):1515–1520, 2007.

[37] Smart and Moore. *Solid State Chemistry*. Taylor and Francis Group, 2005.

[38] A. Holt and P. Kofstad. Electrical-conductivity and defect structure of cr2o3 .2. reduced temperatures (less-than-similar-to-1000-degrees-c). *Solid State Ionics*, 69(2):137–143, 1994.

[39] X. Chen, P. Y. Hou, C. P. Jacobson, S. J. Visco, and L. C. De Jonghe. Protective coating on stainless steel interconnect for sofcs: oxidation kinetics and electrical properties. *Solid State Ionics*, 176(5-6):425–433, 2005.

[40] P. Y. Hou, K. Q. Huang, and W. T. Bakker. Promises and problems with metallic interconnects for reduced temperature solid oxide fuel cells. volume 99 of *Solid Oxide Fuel Cells*, pages 737–748, 1999.

[41] H. Nagai, T. Fujikawa, and K. Shoji. Electrical-conductivity of cr2o3 doped with la2o3, y2o3 and nio. *Transactions of the Japan Institute of Metals*, 24(8):581–588, 1983.

[42] A. Holt and P. Kofstad. Electrical conductivity and defect structure of mg-doped cr2o3. *Solid State Ionics*, 100(3-4):201–209, 1997.

[43] Z. G. Lu, J. H. Zhu, E. A. Payzant, and M. P. Paranthaman. Electrical conductivity of the manganese chromite spinel solid solution. *Journal of the American Ceramic Society*, 88(4):1050–1053, 2005.

[44] Sofia Karlsson. High temperature corrosion of stainless steels, 2011.

[45] Matthew P Dewar. Characterization and evaluation of aged 20cr32ni1nb stainless steels. Master's thesis, University of Alberta, 2013.

[46] K. L. Scrivener. Backscattered electron imaging of cementitious microstructures: understanding and quantification. *Cement & Concrete Composites*, 26(8):935–945, 2004.

[47] J. Froitzheim, S. Canovic, M. Nikumaa, R. Sachitanand, L. G. Johansson, and J. E. Svensson. Long term study of cr evaporation and high temperature corrosion behaviour of co coated ferritic steel for solid oxide fuel cell interconnects. *Journal of Power Sources*, 220:217–227, 2012.

[48] Z. G. Yang, G. G. Xia, C. M. Wang, Z. M. Nie, J. Templeton, J. W. Stevenson, and P. Singh. Investigation of iron-chromium-niobium-titanium ferritic stainless steel for solid oxide fuel cell interconnect applications. *Journal of Power Sources*, 183(2):660–667, 2008.

[49] W. N. Liu, X. Sun, E. Stephens, and M. Khaleel. Interfacial shear strength of oxide scale and ss 441 substrate. *Metallurgical and Materials Transactions a-Physical Metallurgy and Materials Science*, 42A(5):1222–1228, 2011.

[50] N. Shaigan, W. Qu, D. G. Ivey, and W. X. Chen. A review of recent progress in coatings, surface modifications and alloy developments for solid oxide fuel cell ferritic stainless steel interconnects. *Journal of Power Sources*, 195(6):1529–1542, 2010.

[51] I. Belogolovsky, P. Y. Hou, C. P. Jacobson, and S. J. Visco. Chromia scale adhesion on 430 stainless steel: Effect of different surface treatments. *Journal of Power Sources*, 182(1):259–264, 2008.

[52] P. Y. Hou and J. Stringer. The effect of reactive element additions on the selective oxidation, growth and adhesion of chromia scales. *Materials Science and Engineering a-Structural Materials Properties Microstructure and Processing*, 202(1-2):1–10, 1995.

[53] M. Casteel, D. Lewis, P. Willson, and M. Alinger. Ionic conductivity method for measuring vaporized chromium species from solid oxide fuel cell interconnects. *International Journal of Hydrogen Energy*, 37(8):6818–6829, 2012.

[54] P. Wei, M. R. Bateni, and A. Petric. Conversion of copper and manganese metallic films to spinel coating. *Journal of Materials Science*, 47(13):5205–5215, 2012.

[55] S. C. Paulson, M. R. Bateni, P. Wei, A. Petric, and V. I. Birss. *Improving LSM Cathode Performance Using (Cu,Mn)(3)O(4) Spinel Coated UNS430 Ferritic Stainless Steel SOFC Interconnects*, volume 7 of *ECS Transactions*, pages 1097–1106. 2007.

[56] S. Molin, B. Kusz, M. Gazda, and P. Jasinski. Protective coatings for stainless steel for sofc applications. *Journal of Solid State Electrochemistry*, 13(11):1695–1700, 2009.

[57] I. Antepara, I. Villarreal, L. M. Rodriguez-Martinez, N. Lecanda, U. Castro, and A. Laresgoiti. Evaluation of ferritic steels for use as interconnects and porous metal supports in it-sofcs. *Journal of Power Sources*, 151:103–107, 2005.